

Porous Cr₂O₃@C composite derived from metal organic framework in efficient semi-liquid lithium-sulfur battery

Almudena Benitez¹, Vittorio Marangon², Celia Hernández-Rentero¹, Álvaro Caballero¹,

Julián Morales^{1*} and Jusef Hassoun^{2*}

¹ Dpto. Química Inorgánica e Ingeniería Química, Instituto de Química Fina y Nanoquímica, Universidad de Córdoba, 14071, Córdoba, Spain

² Department of Chemical and Pharmaceutical Sciences, University of Ferrara, Via Fossato di Mortara 17, Ferrara 44121, Italy

*Corresponding Authors: iq1mopaj@uco.es, jusef.hassoun@unife.it

Abstract

A carbon composite including Cr₂O₃ (Cr₂O₃@C) and benefitting of a metal organic framework (MOF) precursor is herein synthesized, and originally employed in a semi-liquid lithium-sulfur cell using a catholyte solution formed by Li₂S₈ polysulfide, conducting lithium salt and film forming additive dissolved in diethylene glycol dimethyl ether (DEGDME). The adopted cell configuration may actually allow the porous structure of the MOF derivative to efficiently enable the lithium/sulfur electrochemical process. Thus, structure, chemical composition, morphology and porosity of the composite are investigated by X-ray diffraction, X-ray photoelectron spectroscopy, scanning electron microscopy, and N₂ adsorption/desorption isotherms, respectively. The data reveal a mesoporous material consisting of aggregated nanometric particles (<100 nm) with relatively high BET surface area (170 m² g⁻¹), uniform element distribution, and a carbon content of about 13 wt.%. Cyclic voltammetry of the Cr₂O₃@C in semi-liquid lithium sulfur cell using the catholyte solution shows a reversible reaction with fast kinetics and Li-diffusion coefficient ranging from about 3×10⁻⁸ cm² s⁻¹ at 2.4 V vs. Li/Li⁺, to 1×10⁻⁸ cm² s⁻¹ at 2 V vs. Li/Li⁺. Furthermore, electrochemical impedance spectroscopy reveals a very stable interphase with an impedance below 5 Ω after an activation process promoted by cycling. The semi-liquid Li/S cell operates with remarkable stability and efficiency approaching 100%, delivers a capacity ranging from 900 mAh g⁻¹

¹ at C/10 rate to 780 mAh g⁻¹ at C/3 rate, and performs over 100 charge/discharge cycles with very modest capacity decay.

Keywords: MOF; Cr₂O₃; carbon composite; catholyte; semi-liquid Li/S battery

Introduction

A proper energy policy can drive the modern society for actually improving the life quality. On the other hand, an energy demand principally based on fossil fuels may lead to pollution, excessive emission of greenhouse gasses, and severe environmental challenges affecting health and climate [1,2]. In this view, an efficient and possibly low-cost energy storage is expected to allow the large scale use of environmentally compatible, while discontinuous, renewable energies such as wind and solar, further improve information and communication technologies, and promote the large scale diffusion of “green” applications such as electric vehicles (EVs) [3]. Lithium-ion battery (LIB), one of the most attracting electrochemical energy storage systems, has well promoted during the last decades the worldwide diffusion of portable electronics, smartphones and laptops [3–6]. In its most typical configuration, the LIB is based on insertion or intercalation electrodes such as graphite at the anode and layered transition metal oxide at the cathode, and has energy density ranging from 180 to 250 Wh kg⁻¹ with remarkable number of charge/discharge cycles [3]. The need for increased energy density to fully match the requirements of emergent applications (e.g., for extending the driving range of EVs) and the raise of issues ascribed to the relevant cost and possible toxicity of transition metals such as Co, triggered the research for alternative electrochemical energy storage systems [7,8]. Lithium sulfur (Li/S) battery presently appears as one of the most promising systems in terms of energy content and cycling ability [9], however with still intrinsic gap between fundamental research and practical application [10]. Indeed, Li/S cell has a theoretical specific capacity of 1675 mAh g⁻¹, that is, about one order of magnitude greater than that of common intercalation materials used in LIBs, and a theoretical energy density as high as 2500 Wh kg⁻¹ [11]. Furthermore, sulfur is characterized by a remarkable abundance, relevant environmental compatibility and low cost [12].

These very attracting characteristics may be jeopardized by the low electronic conductivity of sulfur, which has an insulating character, and by the solubility of the Li/S reaction products, that is, the lithium polysulfides, which can shuttle from the cathode to the anode and cause loss of active material and severe limitation of cell efficiency and cycle life [13]. Several strategies, including the use of various carbons [14,15], conductive polymers [16,17], metal oxides [18,19] and nanometric metals [20] into the electrode formulation have been proposed to mitigate these shortcomings. Polypyrrol (PPy)@MnO₂@S with dual core-shell structure exploited the polar MnO₂ hollow spheres to provide inner space for alleviating the volume expansion for sulfur, and to effectively moderate the dissolution of polysulfides by synergistic effect of structural restriction and chemical adsorption, and generate sufficient electrical conduction. The Li/PPy@MnO₂@S cell delivered capacity ranging from about 1400 at 0.1C rate to about 700 mAh g⁻¹ at 1C rate and a capacity decay rate of 0.048% at 0.5C over 500 cycles [21]. Furthermore, MnO₂/GO/CNTs-S composite with three-dimensional architecture was synthesized by a one-pot chemical method and heat treatment. The MnO₂/GO nanosheets anchored on the sidewalls of CNTs had a dual-efficient absorption capability for polysulfide intermediates. The electrode delivered in lithium cell capacity from 1500 mAh g⁻¹ at 0.05C rate to above 900 mAh g⁻¹ at 1C rate [22]. Recently, a bimetallic- organic- framework hosting sulfur nanoparticles exploited porous graphite and cobalt- nickel oxides (C/NiCo₂O₄) to physically and chemically entrap polysulfides, and for enabling electrode conductivity. The composite sulfur cathode delivered in lithium cell an initial specific capacity of about 970 mAh g⁻¹ at 0.5C and final capacity of about 670 mAh g⁻¹ over 500 cycles [23]. Various alternative methods with very promising results were furthermore adopted to prepare sulfur-carbon composites and achieve sulfur anchorage, including *in-situ* deposition at the interspaces between carbon nanoparticles in aqueous solution at room temperature [24], template/casting for achieving flexible and free-standing carbon film using CNTs and graphene [25], clustering in a pomegranate- like structure [26], iron/nitrogen co-doping of graphene [27], and nitrogen- doping of graphene/titanium nitride nanowires [28]. All these synthesis procedures were

devoted to control the complex reaction of the sulfur in lithium cell which unavoidably involves dissolution and re-precipitation of polysulfides and sulfur over the electrodes with various morphological changes, as clearly indicated by a recent study of the reversible conversion of a sulfur–metal nanocomposite combining X-ray computed tomography at the micro- and nanoscales and electrochemistry [29]. Metal organic frameworks (MOFs) with micro- and meso-porosity have been suggested to confine the S particles and efficiently trap polysulfides [30]. Since the first report on the application of these compounds in Li/S batteries, in particular the MIL-100 (Cr) [31], new contributions aimed to improve their performances. In particular, particle size [32], nature of the metallic element and ligand [33,34], and coating with polymers [35] have been considered the most relevant factors for determining the MOFs characteristics in Li/S battery. However, a partially insulating nature and H₂O molecules connected to their framework by different types of bonds have led to a significant drop during cycling and limited the S content in the composite [36,37]. Recently, MOF/S composites with higher conductivity and improved performances have been achieved by using conductive additives such as reduced graphene oxide (rGO) [33,38], graphene nanosheets (GNS) [39], carbon nanotubes (CNT) [40] and conductive polymers, including poly (3,4-ethylenedioxythiophene) polystyrene sulfonate (PEDOT-PSS) [35] and polypyrrol (ppy) [41]. Another approach for enhancing the electrode conductivity, and promoting at the same time the interaction of the electrode host matrix with the polysulfides produced by Li/S reaction, consisted of the use carbon-metal oxide composites obtained from MOFs [30,37,42].

Herein, we extend the latter approach by using a carbon-chromium oxide MOF-derivative in a semi-liquid lithium-sulfur cell [43,44] exploiting the catholyte concept [45]. Composites including Cr₂O₃ and carbon, obtained by different procedures, have been principally used in Li-ion batteries. Indeed, Cr₂O₃/C electrodes have been efficiently used as Li-ion battery anode with enhanced cycling and rate performance compared with pure Cr₂O₃ due to the important role played by the carbon in improving the electrical conductivity of Cr₂O₃, inhibiting the aggregation and acting as a favourable buffer to the volume change during the electrochemical process [46,47]. Furthermore,

various cell using the semi-liquid, lithium-sulfur configuration have been reported and efficiently cycled by exploiting polysulfide containing solutions, indicated so far as *catholyte*. Three-dimensional reduced graphene oxide (3D-rGO) sponge allowed the efficient cycling of a Li_2S_6 catholyte with a capacity of about 1600 mAh g^{-1} at 0.1C, areal capacity of 3.5 mAh cm^{-2} and 98% coulombic efficiency over 200 cycles [48]. A cell exploiting sulfur/meso carbon micro beads (MCMB) electrode and Li_2S_8 containing catholyte efficiently operated by delivering a specific capacity approaching 1500 mAh g^{-1} for over 80 cycles at a C/5 rate, without significant capacity decay and with high coulombic efficiency [49]. A Li_2S_9 solution has also been used as catholyte in semi-liquid lithium-sulfur cell by using a porous carbon electrode as the current collector with a capacity approaching 600 mAh g^{-1} for about 70 cycles [50]. Furthermore, polysulfide has been included in solid membranes and used in a Li/S cell with capacity of about 1200, 1100, and 1000 mAh g^{-1} , respectively, at C/10, C/5, and C/3, however with a significant decay during cycling [51]. Lithium polysulfide has been employed in a flow battery design with embedded current collector networks exhibiting an electrochemical activity distributed throughout the volume of flow electrodes rather than being confined to surfaces of stationary current collectors. The nanoscale network architecture enabled cycling of a polysulfide solutions deep into precipitation regimes at C/4 rate, with an initial capacity of 1200 mAh g^{-1} and a capacity retention of 50% over 100 cycles [52]. These semi-liquid systems based on catholyte have mainly employed a carbon material as the support for the electrochemical process, while the combination of Cr_2O_3 and carbon has never been exploited in a semi-liquid Li/S cell according to the best of our knowledge. Nevertheless, Cr_2O_3 decorating carbon nanofibers were employed as coating in a multifunctional separator for high-performance Li-S batteries using a Li_2S_6 catholyte solution [53].

Therefore, the cell formed in our work by combining the carbon-chromium oxide MOF-derivative ($\text{Cr}_2\text{O}_3@\text{C}$) and the Li_2S_8 catholyte is expected to allow a reversible conversion into lithium and sulfur of Li_2S_8 active polysulfide, dissolved together with a lithium salt and a lithium-protecting additive into diethylene glycol dimethyl ether (DEGDME) [54]. This alternative cell configuration

is suggested as suitable approach to efficiently enable optimized performances of the MOF-derivative composites in Li/S battery.

Experimental Section

Preparation of MIL-101(Cr) and Cr₂O₃@C composite

The MIL-101(Cr) MOFs were prepared by a previously reported method [55,56]. Specifically, 2.0 g (5.0 mmol) of chromium (III) nitrate nonahydrate (Cr(NO₃)₃·9H₂O, Panreac) and 0.55 g (3.3 mmol) of 1,4-benzene dicarboxylic acid (H₂BDC, Sigma Aldrich) were dissolved in 50 mL of deionized water under vigorous stirring for 30 minutes to completely dissolve the dicarboxylic acid. The dark green suspension obtained was transferred to a 100 mL Teflon-lined autoclave. The mixture was sealed, held at 180 °C for 10 h and naturally cooled down to room temperature. Subsequently, MIL-101 was filtered, dipped into distilled water for one day, filtered again, washed several times with ethanol, and dried at 80 °C overnight. Then, as-synthesized MIL-101 was calcined in nitrogen atmosphere at 600 °C for 3 h in a tubular oven at a speed of 10 °C min⁻¹ using a constant gas flow of 50 mL min⁻¹ (preliminary purge was performed at room temperature for 30 min using N₂ flow of 100 mL min⁻¹). The final sample is subsequently indicated by the acronym Cr₂O₃@C.

Electrode preparation

The electrode was prepared by mixing 80 wt.% of Cr₂O₃@C, 10 wt.% of conductive agent (Super P carbon, Timcal) and 10 wt.% of polyvinylidene fluoride (PVDF 6020, Solvay) polymer binder in N-methyl-2-pyrrolidone (NMP, Sigma-Aldrich) to form a slurry. Then, a carbon paper (GDL, ELAT LT1400W, MTI Corp.) was used as substrate and coated with the slurry by doctor blade (MTI Corp.). The electrodes were dried in air for 3 hours at 70 °C by using a hot-plate to remove the solvent, cut into disks of 14-mm diameter, and vacuum dried overnight at 100 °C to remove residual traces of water and solvent before inserting in Ar-filled glovebox (MBraun, O₂ and H₂O content below 1 ppm).

Catholyte preparation

The catholyte was prepared inside Ar-filled glovebox (MBraun, O₂ and H₂O content below 1 ppm) according to our previous paper [54]. Elemental sulfur powder (Sigma-Aldrich) and lithium metal chopped (Rockwood Lithium) were mixed in a molar ratio of 4:1 and dissolved in diethylene glycol dimethyl ether (DEGDME, anhydrous, 99.5%, Sigma-Aldrich) with a final Li₂S₈ ratio of 5 wt.%. Then, the yellow suspension was heated at 80 °C overnight by stirring, and it turned dark red. To ensure the complete reaction between sulfur and lithium, the suspension was stirred for two more days without heating. The catholyte was obtained by adding to the latter solution lithium bis(trifluoromethanesulfonyl)imide (LiTFSI, Sigma-Aldrich) and lithium nitrate (LiNO₃, Sigma-Aldrich) with a ratio of 1 mole of each salt in \approx 1 kg of DEGDME solvent, and stirring for 12 h at room temperature. The catholyte used as a dissolved active material for the Li/S cell is subsequently indicated as DEGDME-Li₂S₈-1m LiNO₃-1m LiTFSI.

Materials Characterization

X-ray diffraction (XRD) patterns were obtained with a Bruker D8 Advance diffractometer using monochromatic Cu K α radiation. The patterns were recorded in the 2 θ range between 5° and 90° at a rate of 10 s per step with step size of 0.02°. Thermogravimetric analysis (TGA) was performed using a Mettler Toledo-TGA/DSC under nitrogen or oxygen atmosphere by heating the sample from 30 to 800 °C at 10 °C min⁻¹. X-ray photoelectron spectroscopy (XPS) measurements were carried out using a SPECS mod. PHOBIOS 150 MCD spectrometer using a Mg K α radiation and a chamber pressure able to reach 4 x 10⁻⁹ mbar. The textural properties were determined by a Micromeritics ASAP 2020 system using nitrogen as adsorbent. Pore size distribution was calculated by the Barret-Joyner-Halenda (BJH) method applied to the adsorption branch of the isotherms. Sample morphologies were investigated by transmission electron microscopy (TEM), employing a Zeiss EM 910 microscope equipped with a tungsten thermoionic electron gun operating at 100 kV, and through scanning electron microscopy (SEM) by means of a JEOL JSM-7800F for the

Cr₂O₃@C and precursor powders, and a Zeiss EVO 40 microscope equipped with a LaB₆ thermoionic electron gun for the Cr₂O₃@C electrode. The SEM was coupled to a microanalysis system for obtaining the energy dispersive X-ray spectra (EDS). SEM images of the Cr₂O₃@C electrode were also obtained at the pristine state and *ex-situ* after a galvanostatic cycling test performed at a constant current rate of C/5 (1C = 1675 mA g⁻¹) in lithium cell (see the next section for further details on the galvanostatic cycling conditions). Prior to the SEM analyses, the electrode was washed with dimethoxy ethane (DME) to remove possible traces of lithium salts, and subsequently dried under vacuum at room temperature for 20 minutes.

Cell assembly and electrochemical measurements

Electrochemical experiments were performed on CR2032 coin-type cells assembled inside an Ar-filled glove box (M-Braun, H₂O and O₂ content below 1 ppm). The cells were prepared by using the disk with 14 mm (1.4 cm) diameter coated by Cr₂O₃@C as the working electrode, a lithium metal disk as the counter/reference electrode and a polyethylene membrane (PE, Celgard) as the separator soaked by 80 μL of the catholyte solution, corresponding to a total sulfur loading of 4.4 mg. Taking into account the electrode geometric area (1.54 cm²) the sulfur surface loading was 2.9 mg cm⁻².

The electrochemical process was studied by cyclic voltammetry (CV) and electrochemical impedance spectroscopy (EIS) tests, which were carried out using a VersaSTAT MC Princeton Applied Research (PAR, AMETEK) analyzer. CV measurements were performed at a constant scan rate of 0.1 mV s⁻¹ within the 1.8–2.8 V range over ten cycles, as well as at scan rates increasing from 0.05 mV s⁻¹, to 0.1, 0.15, 0.2 and 0.25 mV s⁻¹ in order to determinate the lithium-ion diffusion coefficients (D_{Li}). EIS measurements were taken at the OCV, after the first, fifth, and tenth CV cycles in the 500 kHz–100 mHz frequency range using a 10 mV amplitude signal and the resulting Nyquist plots were studied by nonlinear least-squared (NLLSQ) fitting through a Boukamp tool [57]. It is worth mentioning that only fits with a χ^2 of the order of 10⁻⁴ or lower were considered suitable. Galvanostatic cycling tests were carried out within the 1.9–2.8 V range with a MACCOR

series 4000 battery test system using C-rates of C/10, C/8, C/5, and C /3 (1C=1675 mA g⁻¹). Both specific capacity and current rate were referred to the sulfur mass in the catholyte (4.4 mg in the coin cell). The narrower voltage range employed in the galvanostatic cycling tests was chosen in order to limit the formation of short-chain polysulfides, such as Li₂S, which occurs at lower voltage values and can lead to poor performances and short cycle life of the lithium-sulfur cell [13]. Instead, voltammetry has explored a more extended potential range in order to fully characterize the electrochemical process of the semi-liquid sulfur cell using the Cr₂O₃@C composite.

Results and discussion

The changes upon annealing of MIL-101(Cr) precursor to obtain the Cr₂O₃@C composite are detected by XRD and TGA in Figure 1. The XRD pattern of MIL-101(Cr) shown in Fig. 1a reveals the characteristic peaks below 25° of 2θ [31,58]. Above this value, intense peaks not assigned to the MIL-101(Cr) compound are also detected and ascribed to the α-CrOOH phase, thus suggesting the presence in the pristine MOF of a Cr oxy-hydroxide impurity [58]. After heating at 600 °C under N₂ only peaks belonging to the α-Cr₂O₃ phase are detected, while the typical peak of C assigned to (002) planes is not detected at 26.5° of 2θ, thus indicating its amorphous nature ascribed to a mild calcination temperature [59]. The TGA curves of the pristine MOF recorded under N₂ and O₂ atmosphere, respectively, as well as the curve of the Cr₂O₃@C recorded under O₂ atmosphere are shown in Fig. 1b. The TGA curves of MOF under N₂ and O₂ reveal similar weight loss of about 20% below 100 °C, which may be likely ascribed to the loss of physically adsorbed water. The observed weight loss is of about 8 H₂O (molecules per formula unit) higher than that reported by literature for MOFs with the same chemical composition, that is, Cr₃O(OH)(H₂O)₂(BDC)₃ [60]. On the other hand, an amount of adsorbed water as high as 40 % have been already reported in literature [61]. At temperatures higher than 100 °C the weight loss becomes greater in the O₂ atmosphere, being very pronounced around 300 °C where the expected oxidation of the organic matrix occurs. The total weight loss for the MOF precursor is therefore detected at 600 °C to be of about 70% [61]. Considering the theoretical MOF composition, including absorbed water, the

theoretical weight loss should be 68.3 % [60]: the difference with respect to our results (70 %) may be reasonably attributed to the presence of the above mentioned α -CrOOH impurity. The TGA curve recorded under N₂ reveals different kinetics and a lower overall weight loss, that is, of about 57 %, as expected by the missing oxidation of the organic matrix. On the other hand, the TGA curve recorded under O₂ of the Cr₂O₃@C is characterized by weight loss only ascribed to CO₂ evolution, thus indicating a carbon content of about 13 % into the composite. The carbon content observed for the composite is lower than that expected by annealing the MIL-101(Cr) MOF [61], most likely due to a partial volatilization of the organic component during the thermal treatment and to the presence of α -CrOOH impurity in the pristine MOF.

Figure 1

The surface composition of the Cr₂O₃@C composite is analyzed by XPS (Figure 2). The survey spectrum (Fig. 2a) clearly indicates the presence of Cr, C and O elements, along with Al used as the support for measurement. The spectrum of Cr 2p (Fig. 2b) may be resolved into peaks with binding energy values around 576.7 and 686.3 eV assigned to Cr 2p_{3/2} and Cr 2p_{1/2}, respectively, which suggests Cr³⁺ bound to O [62]. Furthermore, the C 1s spectrum (Fig. 2c) can be fitted according to three components located at 284.55 (70.7 %), 286.7 (11.5 %) and 288.9 (17.8 %) eV, assigned to C-C/C=C, C-O epoxy and C-O carboxyl environments, respectively [63]. Finally, the O 1s signal is fitted according to two components at 529.8 and 531.9 eV (Fig. 2d), where the first one is assigned to O²⁻ ions, while the second peak is more complex since it can be assigned to OH⁻ ions or to O⁻ ions, which can compensate deficiencies in the sub-surface of the transition metal oxide [64], and even to adsorbed H₂O [65]. The atomic concentrations calculated by XPS are 23.0, 62.4 and 15.6% for C, O and Cr, respectively. The XPS data indicate relevantly higher amount of O compared to the value estimated by the TGA curves of Cr₂O₃@C, thus suggesting a different surface composition for the sample with respect to the bulk as the XPS mainly focuses at the material surface.

Figure 2

Figure 3 reports the morphology of the composite as detected by SEM, EDS and TEM, as well as its textural properties determined by N₂ adsorption/desorption isotherms. The SEM image of the MOF precursor reported for comparison in Fig. 3a reveals particles having the typical pseudo-octahedral morphology of MIL-101(Cr) with size ranging between 100 nm and 200 nm, in addition to other particles characterized by a more irregular morphology most likely ascribed to the α -CrOOH [58]. In spite, the SEM of the Cr₂O₃@C composite (Fig. 3b) shows a morphology changes after calcination: the pseudo-octahedral morphology almost vanishes by pyrolysis of the organic ligand, being replaced by nanometric particles forming agglomerates (> 100 nm) with remarkably higher surface roughness, and very regular shape compared to the pristine MOF. In addition, the EDS elemental mapping reveals homogeneous C, O, and Cr elements distribution over the Cr₂O₃@C sample (Fig. 3c, d and e, respectively). The TEM images of the Cr₂O₃@C composite (Fig. 3f, g) well support the SEM data (compare with Fig. 3a, b), and show a wide size distribution of agglomerated particles ranging from few nanometers (Fig. 3f) to values approaching 100 nm (Fig. 3g). It is worth mentioning that particle interconnection may be actually promoted by the carbon, which is detected by TGA in Fig. 1b to reach 13% in weight and most likely represented by light grey particles with an irregular shape, such that circled in the TEM image of fig. 3f. The surface area and pore volume of the Cr₂O₃@C composite are determined by N₂ adsorption measurements (Fig 3h, i). The adsorption/desorption isotherm reported in Fig. 3h shows a hysteresis loop at high relative pressure indicating a narrow pore size distribution into the composite, and allows to calculate a BET surface area of 170 m² g⁻¹ and a pore volume of 0.5 cm³ g⁻¹. The pore size distribution (Fig. 3i) mainly indicates a mesoporous structure and an average pore size of 12 nm. It is worth noting that the shape of the isotherms and the specific surface values are in line with those reported for Cr₂O₃@C composites derived from MIL-101(Cr) MOF [66,67]. These values are expected to support an efficient reaction of the dissolved polysulfide in the semi-liquid Li/S cell [54]. Polysulfide-trapping ability of transition metal oxides included in the composition of the cathode support has been indicated in various papers to depend on the anchoring ability of the polar

sites of the oxide, which attract the sulfur and lead to the absorption of dissolved polysulfides [68–71]. In particular, the absorption ability of Cr_2O_3 has been recently demonstrated using nanoparticle decorating carbon fibers derived from solid leather wastes adopted as coating for separator and aimed to achieve high performance lithium-sulfur battery [53]. The absorbent properties of acetylene black (AB) and Cr_2O_3 were measured in the above work using a Li_2S_6 polysulfide solution. Accordingly, polysulfide solutions exposed to AB upgraded by Cr_2O_3 powders turned nearly colorless and transparent, while the bare AB powders had a negligible impact on the color of the solution, thus qualitatively suggesting the polysulfide-trapping ability of the Cr_2O_3 .

Figure 3

Figure 4 reveals the electrochemical features of the $\text{Cr}_2\text{O}_3@\text{C}$ in a lithium cell employing the DEGDME- Li_2S_8 -1m LiNO_3 -1m LiTFSI catholyte [54]. The CV profiles recorded within 1.8-2.8 V at a constant scan rate of 0.1 mV s^{-1} (Fig. 4a) show during the first cathodic scan only one peak below 2 V ascribed to the reduction of Li_2S_8 to short chain polysulfides (e.g., Li_2S_4 , Li_2S_2), while the subsequent anodic scan reveals two defined peaks above 2.4 V ascribed to the oxidation of the short chain polysulfides back to Li_2S_8 and finally to S [54]. The subsequent cycles evidence voltammetry profiles characterized by two reduction peaks around 2 V and 2.4 V during cathodic scan, and two corresponding oxidation peaks above 2.4 V during anodic scan, ascribed to the reversible redox process of S and Li with formation of long- and short-chain polysulfides [72]. Furthermore, the voltage profiles well overlap and the polarization decreases, thus suggesting an optimized electrochemical process, the reversibility of which improves by the ongoing of cycles [54,72]. The electrode/electrolyte interphase evolution of the Li/DEGDME- Li_2S_8 -1m LiNO_3 -1m LiTFSI/ $\text{Cr}_2\text{O}_3@\text{C}$ cell upon voltammetry is detected by EIS upon cycling (Fig. 4b), and the recorded spectra are analysed by NLLSQ fitting (see Experimental section) [57]. The Nyquist plot of the cell in its pristine condition at the open circuit (OCV) can be represented by the $R_e(R_1Q_1)(R_2Q_2)$ equivalent circuit consisting of an electrolyte resistance (R_e) at high frequency values, a well-defined semicircle in the medium-high frequency region accounting for both the solid

electrolyte interphase (SEI) film formed at the electrodes surface and for the faradic charge-transfer (R_1Q_1), and a low-frequency depressed profile accounting for the lithium ion finite-length Warburg diffusion at the electrode/electrolyte interphase (R_2Q_2) [73,74]. After subsequent CV cycles the Nyquist plot shrinks, the impedance remarkably decreases while the profile modifies, particularly in the low-frequency region, being now represented by the new equivalent circuit $R_e(R_1Q_1)Q_2$ [75]. Hence, the depressed profile observed at the OCV at low-frequency modifies after CV cycles to form a tilted line associated with a semi-infinite Warburg element (Q_2) [75,76]. These changes are likely ascribed to the electrochemical activation of the electrode/electrolyte interphase upon the first cycle, and by the ongoing of the redox process which progressively promotes the reversible formation of sulfur and the various polysulfides at the $Cr_2O_3@C$ surface, as indeed observed for this kind of catholyte using a different electrode structure [54]. Accordingly, the electrode/electrolyte interphase resistance obtained from the semicircle width drops from about 60 Ω at OCV to values as low as 4.7 Ω after 10 cycles (see Table 1), which is in line with the CV profiles that suggest progressive improvement of the reactions kinetics by cycling.

Table 1

A further important characteristic of the electrode/electrolyte interphase is represented by the lithium-ion diffusion coefficient D_{Li} which may be obtained from CV measurements performed at various scan rates (Fig. 4c, top) and calculated at the different state of charge (Fig. 4c bottom) using the Randles-Sevcik equation [77–79]:

$$I_p = 2.69 \times 10^5 n^{3/2} A D_{Li}^{0.5} v^{0.5} C_{Li} \quad (1)$$

where I_p is the peak current, n is the number of electrons transferred during the reaction, A is the electrode geometric area, v the scanning rate, and C_{Li} the concentration of lithium ions in the catholyte. According to Eq. (1), D_{Li} may be determined by the slope of the linear plot of I_p vs $v^{0.5}$ both during cathodic and during anodic scans (Fig. 4d). Two peaks, at about 2.4 and 2 V, are considered for D_{Li} calculation during the cathodic scan, while only the major peak above 2.4 V is taken into account during anodic scan since the subsequent minor peak can generally merge into the

latter making problematic the evaluation [72]. Therefore, the values of D_{Li} determined taking into account the above mentioned peaks are of 2.7×10^{-8} , 1.1×10^{-8} , and 2.6×10^{-8} $\text{cm}^2 \text{s}^{-1}$, respectively. These values exceed the ones previously observed for the Li/S cell [72], most likely due to the nature of the cell involving an enhanced carbon/metal oxide substrate and a catholyte instead of a solid electrode.

Figure 4

Galvanostatic discharge–charge experiments were carried out to evaluate the performance of the $\text{Cr}_2\text{O}_3@\text{C}$ composite in the semi-liquid Li/S cell using the DEGDME- Li_2S_8 -1m LiNO_3 -1m LiTFSI catholyte at a current density of C/5 ($1C = 1675 \text{ mA g}^{-1}$) and at various C-rates (Figure 5). The voltage profiles of the cell at C/5 rate (Fig. 5a) show upon the first activation cycle (see discussion of CV in Fig 4a) the two discharge plateaus at about 2.4 and 2 V, corresponding to the reversible reaction of sulfur to form long and short chain polysulfides, respectively, which are reversed during charge into two plateaus at about 2.3 and 2.5 V in line with the CV curves. Furthermore, Fig. 5a indicates that the cell at the steady state can deliver reversibly and with relatively low polarization a specific capacity exceeding 800 mAh g^{-1} . Insights on the cell performances at various currents is given by the cycling profiles of Fig 5b which displays a steady state capacity approaching 900 mAh g^{-1} at C/10 and C/8, exceeding 800 mAh g^{-1} at C/5, and slightly below 800 mAh g^{-1} at C/3 rate. The decrease of the capacity by increasing the C-rate may be ascribed to the increase of the cell polarization by raising currents. Therefore, we can assume that the $\text{Cr}_2\text{O}_3@\text{C}$ composite enables efficient reaction of the semi-liquid lithium sulfur cell and a suitable polysulfides reversible conversion from C/10 to C/3 rate, with capacity ranging from 800 to 900 mAh g^{-1} , that is, a moderate range of operation in line with similar cell configuration [54,80]. Remarkably, the cell cycled at C/5 holds almost its steady state capacity of about 800 mAh g^{-1} with only limited signs of decay for 100 charge/discharge cycles, and retains a Coulombic efficiency approaching 100% over the whole cycling test (Fig. 5c).

Figure 5

The structural and morphological retention of the $\text{Cr}_2\text{O}_3@\text{C}$ electrode is investigated in Figure 6 by *ex-situ* SEM/EDS and XRD analyses performed before and after cycling at C/5 rate ($1\text{C} = 1675 \text{ mA g}^{-1}$). The SEM of the pristine electrode (Fig. 6a) shows that the heterogeneous morphology of the material remains almost unchanged upon cycling (Fig. 6b), while the brightness of the image intensifies as most likely due to the insulating character of traces of sulfur crystallized on the surface during the electrochemical process. This speculation is fully supported by the EDS elemental map reported in inset in Fig. 6b, which shows sulfur atoms uniformly distributed on the electrode surface after cycling. Furthermore, the structural stability of the material upon cycling is highlighted by the XRD analyses of Fig. 6c which evidence the retention of the $\alpha\text{-Cr}_2\text{O}_3$ phase upon operating in Li/S cell, and the absence of undesired by-products formation, thus suggesting the inert nature of the $\text{Cr}_2\text{O}_3@\text{C}$ composite. Therefore, these remarkable features, as well as the promising electrochemical performances, suggest the $\text{Cr}_2\text{O}_3@\text{C}$ composite as a suitable electrode material for application in alternative Li/S cell configuration such as the semi-liquid one investigated in this work.

Figure 6

Conclusions

In summary, a composite $\text{Cr}_2\text{O}_3@\text{C}$ has been synthesized from MIL-101(Cr) MOF, characterized by various chemical-physical techniques and successfully employed as the electrode support for the Li/S reaction in a semi-liquid cell employing a DEGDME-Li₂S₈-1m LiNO₃-1m LiTFSI catholyte. The composite revealed a morphology consisting of agglomerated mesoporous particles with a size below 100 nm, homogeneous C, O, and Cr elements distribution, a BET surface area as high as $170 \text{ m}^2 \text{ g}^{-1}$ and a pore volume of $0.5 \text{ cm}^3 \text{ g}^{-1}$. Furthermore, the test revealed that the composite is predominantly formed by Cr_2O_3 with a carbon weight ratio of about 13% due to the preparation technique which involved calcination in a nitrogen atmosphere at $600 \text{ }^\circ\text{C}$ and avoided oxidizing condition. On the other hand, bare Cr_2O_3 samples without carbon, not considered herein, may partially have semiconductor character, with a gap band of 3.3 eV [81], which is achieved both by

oxidizing and reducing conditions as well as by doping with other oxides such as TiO₂ to create defects and increase the mobility of carriers [82]. The Cr₂O₃@C material enabled the reversible Li₂S₈ conversion to short chain polysulfides and back to sulfur with efficient kinetics and potentials ranging from about 2 V to above 2.4 V vs. Li⁺/Li. This performance was attributed to an enhanced electrode/electrolyte interphase characterized by resistance values below 5 Ω upon an electrochemical activation process, and a diffusion coefficient exceeding 10⁻⁸ cm² s⁻¹ at the various states of the charge. The Li/S semi-liquid cell has operated between C/10 and C/3 current rate with a specific capacity ranging from about 900 mAh g⁻¹ to values slightly below 800 mAh g⁻¹. Furthermore, the battery revealed remarkable stability, and a Coulombic efficiency approaching 100% at the steady state, while *ex-situ* SEM and XRD analyses evidenced the retention of both the electrode morphology and structure upon cycling. These findings well suggest the Cr₂O₃@C composite as suitable electrode for application in the alternative, semi-liquid lithium sulfur cell configuration.

Acknowledgements

This work was funded by the grant “Fondo di Ateneo per la Ricerca Locale (FAR) 2019”, University of Ferrara, within the collaboration project “Accordo di Collaborazione Quadro 2015” between University of Ferrara (Chemical and Pharmaceutical Sciences Department) and Sapienza University of Rome (Chemistry Department). The research was also funded by Ministerio de Economía y Competitividad (Project MAT2017-87541-R) and Junta de Andalucía (Group FQM-175).

References

- [1] J. Chen, C. Li, Z. Ristovski, A. Milic, Y. Gu, M.S. Islam, et al., A review of biomass burning: Emissions and impacts on air quality, health and climate in China, *Sci. Total Environ.* 579 (2017) 1000–1034. doi:10.1016/j.scitotenv.2016.11.025.
- [2] C.D. Thomas, A. Cameron, R.E. Green, M. Bakkenes, L.J. Beaumont, Y.C. Collingham, et

- al., Extinction risk from climate change, *Nature*. 427 (2004) 145–148.
doi:10.1038/nature02121.
- [3] D. Di Lecce, R. Verrelli, J. Hassoun, Lithium-ion batteries for sustainable energy storage: Recent advances towards new cell configurations, *Green Chem.* 19 (2017) 3442–3467.
doi:10.1039/c7gc01328k.
- [4] B. Scrosati, Recent advances in lithium ion battery materials, *Electrochim. Acta.* 45 (2000) 2461–2466. doi:10.1016/S0013-4686(00)00333-9.
- [5] B. Scrosati, J. Hassoun, *Lithium batteries: Current technologies and future trends*, 2012.
doi:10.1533/9780857096371.4.573.
- [6] J.L. Sullivan, L. Gaines, Status of life cycle inventories for batteries, *Energy Convers. Manag.* 58 (2012) 134–148. doi:10.1016/j.enconman.2012.01.001.
- [7] A. Yoshino, Development of the Lithium-Ion Battery and Recent Technological Trends, in: G. Pistoia (Ed.), *Lithium-Ion Batter.*, Elsevier, 2014: pp. 1–20. doi:10.1016/B978-0-444-59513-3.00001-7.
- [8] J.B. Goodenough, Electrochemical energy storage in a sustainable modern society, *Energy Environ. Sci.* 7 (2014) 14–18. doi:10.1039/c3ee42613k.
- [9] L. Carbone, S.G. Greenbaum, J. Hassoun, Lithium sulfur and lithium oxygen batteries: new frontiers of sustainable energy storage, 1 (2017) 228–247. doi:10.1039/C6SE00124F.
- [10] R. Fang, S. Zhao, Z. Sun, D.-W. Wang, H.-M. Cheng, F. Li, More Reliable Lithium-Sulfur Batteries: Status, Solutions and Prospects, *Adv. Mater.* 29 (2017) 1606823.
doi:10.1002/adma.201606823.
- [11] J. Kim, D.-J. Lee, H.-G. Jung, Y.-K. Sun, J. Hassoun, B. Scrosati, An Advanced Lithium-Sulfur Battery, *Adv. Funct. Mater.* 23 (2013) 1076–1080. doi:10.1002/adfm.201200689.
- [12] L. Ma, K.E. Hendrickson, S. Wei, L.A. Archer, Nanomaterials: Science and applications in the lithium-sulfur battery, *Nano Today*. 10 (2015) 315–338.
doi:10.1016/j.nantod.2015.04.011.

- [13] C. Barchasz, J.C. Leprêtre, F. Alloin, S. Patoux, New insights into the limiting parameters of the Li/S rechargeable cell, *J. Power Sources*. 199 (2012) 322–330.
doi:10.1016/j.jpowsour.2011.07.021.
- [14] N. Moreno, A. Caballero, L. Hernán, J. Morales, J. Canales-Vázquez, Ordered mesoporous carbons obtained by a simple soft template method as sulfur immobilizers for lithium-sulfur cells, *Phys. Chem. Chem. Phys.* 16 (2014) 17332–17340. doi:10.1039/c4cp02829e.
- [15] R. Wu, S. Chen, J. Deng, X. Huang, Y. Song, R. Gan, et al., Hierarchically porous nitrogen-doped carbon as cathode for lithium–sulfur batteries, *J. Energy Chem.* 27 (2018) 1661–1667.
doi:10.1016/j.jechem.2018.02.010.
- [16] Y. Yang, G. Yu, J.J. Cha, H. Wu, M. Vosgueritchian, Y. Yao, et al., Improving the performance of lithium-sulfur batteries by conductive polymer coating, *ACS Nano*. 5 (2011) 9187–9193. doi:10.1021/nn203436j.
- [17] G. Ma, F. Huang, Z. Wen, Q. Wang, X. Hong, J. Jin, et al., Enhanced performance of lithium sulfur batteries with conductive polymer modified separators, *J. Mater. Chem. A*. 4 (2016) 16968–16974. doi:10.1039/C6TA07198H.
- [18] Z. Wei Seh, W. Li, J.J. Cha, G. Zheng, Y. Yang, M.T. McDowell, et al., Sulphur–TiO₂ yolk–shell nanoarchitecture with internal void space for long-cycle lithium–sulphur batteries, *Nat. Commun.* 4 (2013) 1331. doi:10.1038/ncomms2327.
- [19] F. Luna-Lama, C. Hernández-Rentero, A. Caballero, J. Morales, Biomass-derived carbon/ γ -MnO₂ nanorods/S composites prepared by facile procedures with improved performance for Li/S batteries, *Electrochim. Acta*. 292 (2018) 522–531. doi:10.1016/j.electacta.2018.09.176.
- [20] V. Marangon, J. Hassoun, Sulfur Loaded by Nanometric Tin as a New Electrode for High- Performance Lithium/Sulfur Batteries, *Energy Technol.* 7 (2019) 1900081.
doi:10.1002/ente.201900081.
- [21] Y. Li, B. Shi, W. Liu, R. Guo, H. Pei, D. Ye, et al., Hollow polypyrrole @ MnO₂ spheres as nano-sulfur hosts for improved lithium-sulfur batteries, *Electrochim. Acta*. 260 (2018) 912–

920. doi:10.1016/j.electacta.2017.12.068.

- [22] Y. Li, D. Ye, W. Liu, B. Shi, R. Guo, H. Zhao, et al., A MnO₂/Graphene Oxide/Multi-Walled Carbon Nanotubes-Sulfur Composite with Dual-Efficient Polysulfide Adsorption for Improving Lithium-Sulfur Batteries, *ACS Appl. Mater. Interfaces*. 8 (2016) 28566–28573. doi:10.1021/acsami.6b04270.
- [23] X. Zhang, Y. Fan, M.A. Khan, H. Zhao, D. Ye, J. Wang, et al., Co–Ni Binary- Metal Oxide Coated with Porous Carbon Derived from Metal- Organic Framework as Host of Nano- Sulfur for Lithium- Sulfur Batteries, *Batter. Supercaps*. 3 (2020) 108–116. doi:10.1002/batt.201900121.
- [24] Y.-S. Su, A. Manthiram, A facile in situ sulfur deposition route to obtain carbon-wrapped sulfur composite cathodes for lithium-sulfur batteries, *Electrochim. Acta*. 77 (2012) 272–278. doi:10.1016/j.electacta.2012.06.002.
- [25] M. Li, W. Wahyudi, P. Kumar, F. Wu, X. Yang, H. Li, et al., Scalable Approach To Construct Free-Standing and Flexible Carbon Networks for Lithium–Sulfur Battery, *ACS Appl. Mater. Interfaces*. 9 (2017) 8047–8054. doi:10.1021/acsami.6b12546.
- [26] W. Li, Z. Liang, Z. Lu, H. Yao, Z.W. Seh, K. Yan, et al., A Sulfur Cathode with Pomegranate-Like Cluster Structure, *Adv. Energy Mater*. 5 (2015). doi:10.1002/aenm.201500211.
- [27] L. Zhang, P. Liang, X.-L. Man, D. Wang, J. Huang, H.-B. Shu, et al., Fe, N co-doped graphene as a multi-functional anchor material for lithium-sulfur battery, *J. Phys. Chem. Solids*. 126 (2019) 280–286. doi:10.1016/j.jpcs.2018.11.027.
- [28] Z. Li, Q. He, X. Xu, Y. Zhao, X. Liu, C. Zhou, et al., A 3D Nitrogen-Doped Graphene/TiN Nanowires Composite as a Strong Polysulfide Anchor for Lithium–Sulfur Batteries with Enhanced Rate Performance and High Areal Capacity, *Adv. Mater*. 30 (2018). doi:10.1002/adma.201804089.
- [29] V. Marangon, D. Di Lecce, F. Orsatti, D.J.L. Brett, P.R. Shearing, J. Hassoun, Investigating

- high-performance sulfur–metal nanocomposites for lithium batteries, *Sustain. Energy Fuels*. 4 (2020) 2907–2923. doi:10.1039/D0SE00134A.
- [30] S. Kuyuldar, D.T. Genna, C. Burda, On the potential for nanoscale metal–organic frameworks for energy applications, *J. Mater. Chem. A*. 7 (2019) 21545–21576. doi:10.1039/C9TA09896H.
- [31] R. Demir-Cakan, M. Morcrette, F. Nouar, C. Davoisne, T. Devic, D. Gonbeau, et al., Cathode Composites for Li–S Batteries via the Use of Oxygenated Porous Architectures, *J. Am. Chem. Soc.* 133 (2011) 16154–16160. doi:10.1021/ja2062659.
- [32] X.-J. Hong, T.-X. Tan, Y.-K. Guo, X.-Y. Tang, J.-Y. Wang, W. Qin, et al., Confinement of polysulfides within bi-functional metal–organic frameworks for high performance lithium–sulfur batteries, *Nanoscale*. 10 (2018) 2774–2780. doi:10.1039/C7NR07118C.
- [33] Y. Hou, H. Mao, L. Xu, MIL-100(V) and MIL-100(V)/rGO with various valence states of vanadium ions as sulfur cathode hosts for lithium-sulfur batteries, *Nano Res.* 10 (2017) 344–353. doi:10.1007/s12274-016-1326-0.
- [34] J. Zhou, R. Li, X. Fan, Y. Chen, R. Han, W. Li, et al., Rational design of a metal–organic framework host for sulfur storage in fast, long-cycle Li–S batteries, *Energy Environ. Sci.* 7 (2014) 2715. doi:10.1039/C4EE01382D.
- [35] W.-W. Jin, H.-J. Li, J.-Z. Zou, S.-Z. Zeng, Q.-D. Li, G.-Z. Xu, et al., Conducting polymer-coated MIL-101/S composite with scale-like shell structure for improving Li–S batteries, *RSC Adv.* 8 (2018) 4786–4793. doi:10.1039/C7RA12800B.
- [36] P.M. Shanthi, P.J. Hanumantha, B. Gattu, M. Sweeney, M.K. Datta, P.N. Kumta, Understanding the Origin of Irreversible Capacity loss in Non-Carbonized Carbonate – based Metal Organic Framework (MOF) Sulfur hosts for Lithium – Sulfur battery, *Electrochim. Acta*. 229 (2017) 208–218. doi:10.1016/j.electacta.2017.01.115.
- [37] Y. Zheng, S. Zheng, H. Xue, H. Pang, Metal–organic frameworks for lithium–sulfur batteries, *J. Mater. Chem. A*. 7 (2019) 3469–3491. doi:10.1039/C8TA11075A.

- [38] W. Bao, Z. Zhang, Y. Qu, C. Zhou, X. Wang, J. Li, Confine sulfur in mesoporous metal–organic framework @ reduced graphene oxide for lithium sulfur battery, *J. Alloys Compd.* 582 (2014) 334–340. doi:10.1016/j.jallcom.2013.08.056.
- [39] Z. Zhao, S. Wang, R. Liang, Z. Li, Z. Shi, G. Chen, Graphene-wrapped chromium–MOF(MIL-101)/sulfur composite for performance improvement of high-rate rechargeable Li–S batteries, *J. Mater. Chem. A.* 2 (2014) 13509–13512. doi:10.1039/C4TA01241K.
- [40] H. Zhang, W. Zhao, M. Zou, Y. Wang, Y. Chen, L. Xu, et al., 3D, Mutually Embedded MOF@Carbon Nanotube Hybrid Networks for High-Performance Lithium-Sulfur Batteries, *Adv. Energy Mater.* 8 (2018) 1800013. doi:10.1002/aenm.201800013.
- [41] H. Jiang, X.-C. Liu, Y. Wu, Y. Shu, X. Gong, F.-S. Ke, et al., Metal-Organic Frameworks for High Charge-Discharge Rates in Lithium-Sulfur Batteries, *Angew. Chemie Int. Ed.* 57 (2018) 3916–3921. doi:10.1002/anie.201712872.
- [42] Q. Wu, X. Zhou, J. Xu, F. Cao, C. Li, Carbon-based derivatives from metal-organic frameworks as cathode hosts for Li–S batteries, *J. Energy Chem.* 38 (2019) 94–113. doi:10.1016/j.jechem.2019.01.005.
- [43] Y. Yang, G. Zheng, Y. Cui, A membrane-free lithium/polysulfide semi-liquid battery for large-scale energy storage, *Energy Environ. Sci.* 6 (2013) 1552. doi:10.1039/c3ee00072a.
- [44] M. Agostini, D.-J.J. Lee, B. Scrosati, Y.K. Sun, J. Hassoun, Characteristics of Li₂S₈-tetraglyme catholyte in a semi-liquid lithium–sulfur battery, *J. Power Sources.* 265 (2014) 14–19. doi:10.1016/j.jpowsour.2014.04.074.
- [45] S. Phadke, E. Coadou, M. Anouti, Catholyte Formulations for High-Energy Li–S Batteries, *J. Phys. Chem. Lett.* 8 (2017) 5907–5914. doi:10.1021/acs.jpcllett.7b02936.
- [46] B. Guo, M. Chi, X.-G. Sun, S. Dai, Mesoporous carbon–Cr₂O₃ composite as an anode material for lithium ion batteries, *J. Power Sources.* 205 (2012) 495–499. doi:10.1016/j.jpowsour.2012.01.092.
- [47] Z. Cao, C. Zuo, Cr₂O₃/carbon nanosheet composite with enhanced performance for

- lithium ion batteries, *RSC Adv.* 7 (2017) 40243–40248. doi:10.1039/C7RA06188A.
- [48] P. Chiochan, S. Kosasang, N. Ma, S. Duangdangchote, P. Suktha, M. Sawangphruk, Confining Li₂S₆ catholyte in 3D graphene sponge with ultrahigh total pore volume and oxygen-containing groups for lithium-sulfur batteries, *Carbon N. Y.* 158 (2020) 244–255. doi:10.1016/j.carbon.2019.12.015.
- [49] D.J. Lee, M. Agostini, J.W. Park, Y.K. Sun, J. Hassoun, B. Scrosati, Progress in lithium-sulfur batteries: The effective role of a polysulfide-added electrolyte as buffer to prevent cathode dissolution, *ChemSusChem.* 6 (2013) 2245–2248. doi:10.1002/cssc.201300313.
- [50] S.S. Zhang, J.A. Read, A new direction for the performance improvement of rechargeable lithium/sulfur batteries, *J. Power Sources.* 200 (2012) 77–82. doi:10.1016/j.jpowsour.2011.10.076.
- [51] X. Yu, Z. Bi, F. Zhao, A. Manthiram, Hybrid Lithium–Sulfur Batteries with a Solid Electrolyte Membrane and Lithium Polysulfide Catholyte, *ACS Appl. Mater. Interfaces.* 7 (2015) 16625–16631. doi:10.1021/acsami.5b04209.
- [52] F.Y. Fan, W.H. Woodford, Z. Li, N. Baram, K.C. Smith, A. Helal, et al., Polysulfide Flow Batteries Enabled by Percolating Nanoscale Conductor Networks, *Nano Lett.* 14 (2014) 2210–2218. doi:10.1021/nl500740t.
- [53] Y. Guan, X. Liu, N. Akhtar, A. Wang, W. Wang, H. Zhang, et al., Cr₂O₃ Nanoparticle Decorated Carbon Nanofibers Derived from Solid Leather Wastes for High Performance Lithium-Sulfur Battery Separator Coating, *J. Electrochem. Soc.* 166 (2019) A1671–A1676. doi:10.1149/2.1181908jes.
- [54] D. Di Lecce, V. Marangon, A. Benítez, Á. Caballero, J. Morales, E. Rodríguez-Castellón, et al., High capacity semi-liquid lithium sulfur cells with enhanced reversibility for application in new-generation energy storage systems, *J. Power Sources.* 412 (2019) 575–585. doi:10.1016/j.jpowsour.2018.11.068.
- [55] W. Liu, J. Huang, Q. Yang, S. Wang, X. Sun, W. Zhang, et al., Multi-shelled Hollow Metal-

Organic Frameworks, *Angew. Chemie Int. Ed.* 56 (2017) 5512–5516.

doi:10.1002/anie.201701604.

- [56] J. Gu, X. Yin, X. Bo, L. Guo, High Performance Electrocatalyst Based on MIL-101(Cr)/Reduced Graphene Oxide Composite: Facile Synthesis and Electrochemical Detections, *ChemElectroChem*. 5 (2018) 2893–2901. doi:10.1002/celec.201800588.
- [57] B. BOUKAMP, A package for impedance/admittance data analysis, *Solid State Ionics*. 18–19 (1986) 136–140. doi:10.1016/0167-2738(86)90100-1.
- [58] H.M. Gobara, R.S. Mohamed, S.A. Hassan, F.H. Khalil, M.S. El-Sall, Pt and Ni Nanoparticles Anchored into Metal–Organic Frameworks MIL-101 (Cr) as Swift Catalysts for Ethanol Dehydration, *Catal. Letters*. 146 (2016) 1875–1885. doi:10.1007/s10562-016-1826-2.
- [59] F.J. Soler-Piña, C. Hernández-Rentero, A. Caballero, J. Morales, E. Rodríguez-Castellón, J. Canales-Vázquez, Highly graphitized carbon nanosheets with embedded Ni nanocrystals as anode for Li-ion batteries, *Nano Res.* 13 (2020) 86–94. doi:10.1007/s12274-019-2576-4.
- [60] S. Liu, F. Xu, L.-T. Liu, Y.-L. Zhou, W. Zhao, Heat capacities and thermodynamic properties of Cr-MIL-101, *J. Therm. Anal. Calorim.* 129 (2017) 509–514. doi:10.1007/s10973-017-6168-9.
- [61] M.-L. Chen, S.-Y. Zhou, Z. Xu, L. Ding, Y.-H. Cheng, Metal-Organic Frameworks of MIL-100(Fe, Cr) and MIL-101(Cr) for Aromatic Amines Adsorption from Aqueous Solutions, *Molecules*. 24 (2019) 3718. doi:10.3390/molecules24203718.
- [62] D. Briggs, *Handbook of X-ray Photoelectron Spectroscopy* C. D. Wanger, W. M. Riggs, L. E. Davis, J. F. Moulder and G. E. Muilenberg Perkin-Elmer Corp., Physical Electronics Division, Eden Prairie, Minnesota, USA, 1979. 190 pp. \$195, *Surf. Interface Anal.* 3 (1981) v–v. doi:10.1002/sia.740030412.
- [63] A. Benítez, A. Caballero, J. Morales, J. Hassoun, E. Rodríguez-Castellón, J. Canales-Vázquez, Physical activation of graphene: An effective, simple and clean procedure for

- obtaining microporous graphene for high-performance Li/S batteries, *Nano Res.* 12 (2019) 759–766. doi:10.1007/s12274-019-2282-2.
- [64] J.-C. Dupin, D. Gonbeau, P. Vinatier, A. Levasseur, Systematic XPS studies of metal oxides, hydroxides and peroxides, *Phys. Chem. Chem. Phys.* 2 (2000) 1319–1324. doi:10.1039/a908800h.
- [65] J.R. Hoenigman, R.G. Keil, An XPS study of the adsorption of oxygen and water vapor on clean lithium films, *Appl. Surf. Sci.* 18 (1984) 207–222. doi:10.1016/0378-5963(84)90045-X.
- [66] Z. Wang, M. Li, Y. Ye, Y. Yang, Y. Lu, X. Ma, et al., MOF-derived binary mixed carbon/metal oxide porous materials for constructing simultaneous determination of hydroquinone and catechol sensor, *J. Solid State Electrochem.* 23 (2019) 81–89. doi:10.1007/s10008-018-4111-z.
- [67] A. Farisabadi, M. Moradi, S. Hajati, M.A. Kiani, J.P. Espinos, Controlled thermolysis of MIL-101(Fe, Cr) for synthesis of Fe_xO_y /porous carbon as negative electrode and Cr_2O_3 /porous carbon as positive electrode of supercapacitor, *Appl. Surf. Sci.* 469 (2019) 192–203. doi:10.1016/j.apsusc.2018.11.053.
- [68] X. Liu, J.-Q. Huang, Q. Zhang, L. Mai, Nanostructured Metal Oxides and Sulfides for Lithium-Sulfur Batteries, *Adv. Mater.* 29 (2017) 1601759. doi:10.1002/adma.201601759.
- [69] X. Tao, J. Wang, C. Liu, H. Wang, H. Yao, G. Zheng, et al., Balancing surface adsorption and diffusion of lithium-polysulfides on nonconductive oxides for lithium-sulfur battery design, 2016. doi:10.1038/ncomms11203.
- [70] X. Tao, J. Wang, Z. Ying, Q. Cai, G. Zheng, Y. Gan, et al., Strong Sulfur Binding with Conducting Magnéli-Phase $\text{Ti}_n\text{O}_{2n-1}$ Nanomaterials for Improving Lithium–Sulfur Batteries, *Nano Lett.* 14 (2014) 5288–5294. doi:10.1021/nl502331f.
- [71] X. Liang, C. Hart, Q. Pang, A. Garsuch, T. Weiss, L.F. Nazar, A highly efficient polysulfide mediator for lithium–sulfur batteries, *Nat. Commun.* 6 (2015) 5682.

doi:10.1038/ncomms6682.

- [72] L. Carbone, T. Coneglian, M. Gobet, S. Munoz, M. Devany, S. Greenbaum, et al., A simple approach for making a viable, safe, and high-performances lithium-sulfur battery, *J. Power Sources*. 377 (2018) 26–35. doi:10.1016/j.jpowsour.2017.11.079.
- [73] D.R. Franceschetti, J.R. Macdonald, R.P. Buck, Interpretation of finite-length-warburg-type impedances in supported and unsupported electrochemical cells with kinetically reversible electrodes, *J. Electrochem. Soc.* 138 (1991) 1368–1371. doi:10.1149/1.2085788.
- [74] L. Carbone, D. Di Lecce, M. Gobet, S. Munoz, M. Devany, S. Greenbaum, et al., Relevant Features of a Triethylene Glycol Dimethyl Ether-Based Electrolyte for Application in Lithium Battery, *ACS Appl. Mater. Interfaces*. 9 (2017) 17085–17095. doi:10.1021/acsami.7b03235.
- [75] T.Q. Nguyen, C. Breitkopf, Determination of Diffusion Coefficients Using Impedance Spectroscopy Data, *J. Electrochem. Soc.* 165 (2018) E826–E831. doi:10.1149/2.1151814jes.
- [76] D. Di Lecce, V. Gancitano, J. Hassoun, Investigation of Mn and Fe Substitution Effects on the Characteristics of High-Voltage $\text{LiCo}_{1-x}\text{M}_x\text{PO}_4$ ($x = 0.1, 0.4$) Cathodes Prepared by Sol–gel Route, *ACS Sustain. Chem. Eng.* 8 (2020) 278–289. doi:10.1021/acssuschemeng.9b05325.
- [77] J.E.B. Randles, A cathode ray polarograph. Part II.—The current-voltage curves, *Trans. Faraday Soc.* 44 (1948) 327–338. doi:10.1039/TF9484400327.
- [78] A. Ševčík, Oscillographic polarography with periodical triangular voltage, *Collect. Czechoslov. Chem. Commun.* 13 (1948) 349–377. doi:10.1135/cccc19480349.
- [79] D. Di Lecce, J. Hassoun, Lithium Transport Properties in $\text{LiMn}_{1-\alpha}\text{Fe}_\alpha\text{PO}_4$ Olivine Cathodes, *J. Phys. Chem. C*. 119 (2015) 20855–20863. doi:10.1021/acs.jpcc.5b06727.
- [80] S. Kim, H. Song, Y. Jeong, Flexible catholyte@carbon nanotube film electrode for high-performance lithium sulfur battery, *Carbon N. Y.* 113 (2017) 371–378. doi:10.1016/j.carbon.2016.11.019.

- [81] A. HOLT, P. KOFSTAD, Electrical conductivity and defect structure of Cr₂O₃. I. High temperatures (>~1000°C), *Solid State Ionics*. 69 (1994) 127–136. doi:10.1016/0167-2738(94)90401-4.
- [82] A. Holt, Electrical conductivity of Cr₂O₃ doped with TiO₂, *Solid State Ionics*. 117 (1999) 21–25. doi:10.1016/S0167-2738(98)00244-6.

List of tables

Table 1. NLLSQ analyses performed on the Nyquist plots reported in Fig. 4b. The impedance spectra were recorded by EIS upon CV, carried out on a Li/DEGDME-Li₂S₈-1m LiNO₃-1m LiTFSI/Cr₂O₃@C cell. See experimental section for samples' acronym.

List of figures

Figure 1. (a) X-ray diffraction (XRD) patterns of MIL-101 (Cr) MOF (cyan) and Cr₂O₃@C (black) composites; reference data of CrOOH (black stars, PDF # 25-1437) and Cr₂O₃ (red stars, PDF # 38-1479) are also reported for comparison. (b) Thermogravimetric analyses (TGA) curves of MIL-101 (Cr) MOF in N₂ and O₂ atmosphere (cyan) and Cr₂O₃@C in O₂ atmosphere (black). See experimental section for samples' acronym.

Figure 2. (a) X-ray photoelectron spectroscopy (XPS) survey spectra of MIL-101 (Cr) MOF (cyan) and Cr₂O₃@C (black) composites, and (b) Cr 2p, (c) C 1s and (d) O 1s deconvoluted XPS spectra of Cr₂O₃@C composite. See experimental section for samples' acronym.

Figure 3. (a,b) Scanning electron microscopy (SEM) images of MIL-101 (Cr) MOF (a) before and (b) after heating treatment, and (c-e) energy dispersion spectroscopy (EDS) elemental maps of Cr₂O₃@C composite. (f,g) Transmission electron microscopy (TEM) images of the Cr₂O₃@C powder; red circle in panel (f) highlights a carbon particle. (h) N₂ adsorption/desorption isotherms and (i) pore size distribution obtained through BJH method of Cr₂O₃@C composite. See experimental section for samples' acronym.

Figure 4. (a) Cyclic voltammetry (CV) measurement performed on a Li/DEGDME-Li₂S₈-1m LiNO₃-1m LiTFSI/Cr₂O₃@C cell at the constant scan rate of 0.1 mV s⁻¹ and (b) Nyquist plots recorded by electrochemical impedance spectroscopy (EIS) at the open circuit voltage (OCV) of the cell and after 1, 5 and 10 cycles (inset shows magnification). CV potential range: 1.8 – 2.8 V; EIS frequency range: 500 kHz – 100 mHz; EIS signal amplitude: 10 mV. (c) CV measurement performed on a Li/DEGDME-Li₂S₈-1m LiNO₃-1m LiTFSI/Cr₂O₃@C cell at various scan rates, that

is, 0.05, 0.1, 0.15, 0.2 and 0.25 mV s^{-1} (top panel) and corresponding lithium diffusion coefficients (D_{Li}) calculated through Randles-Sevcik equation (1) [77–79] (bottom panel). **(d)** Linear fitting of the peak currents obtained from the voltammograms reported in panel (c). CV potential range: 1.8 – 2.8 V. See experimental section for samples' acronym.

Figure 5. (a,b) Selected voltage profiles of the galvanostatic cycling measurement performed on a Li/DEGDME-Li₂S₈-1m LiNO₃-1m LiTFSI/Cr₂O₃@C cell (a) at the constant C-rate of C/5 (panel (c) shows the corresponding cycling trend and coulombic efficiency) and (b) at increasing C-rates, that is, C/10, C/8, C/5 and C/3 (1C = 1675 mA g^{-1}). Voltage range: 1.9 – 2.8 V. See experimental section for samples' acronym.

Figure 6. (a,b) Scanning electron microscopy (SEM) images of the Cr₂O₃@C electrode (a) at the pristine state and (b) after 7 cycles at C/5 (1C = 1675 mA g^{-1}) in a cell exploiting the Li/DEGDME-Li₂S₈-1m LiNO₃-1m LiTFSI/Cr₂O₃@C configuration. Voltage range: 1.9 – 2.8 V. Inset in panel (b) displays the corresponding energy dispersion spectroscopy (EDS) elemental map for sulfur. **(c)** X-ray diffraction (XRD) patterns of the Cr₂O₃@C electrode at the pristine state (dark green) and after the galvanostatic cycling test (black); reference data of Cr₂O₃ (light green, PDF # 38-1479) are also reported for comparison.

Cell condition	Circuit	R_1 [Ω]	χ^2
OCV	$R_e(R_1Q_1)(R_2Q_2)$	60 ± 2	2.7×10^{-4}
1 CV cycle	$R_e(R_1Q_1)$	10 ± 0.2	4.0×10^{-4}
5 CV cycles	$R_e(R_1Q_1)Q_2$	3.5 ± 0.1	1.5×10^{-4}
10 CV cycles	$R_e(R_1Q_1)Q_2$	4.7 ± 0.1	5.9×10^{-5}

Table 1

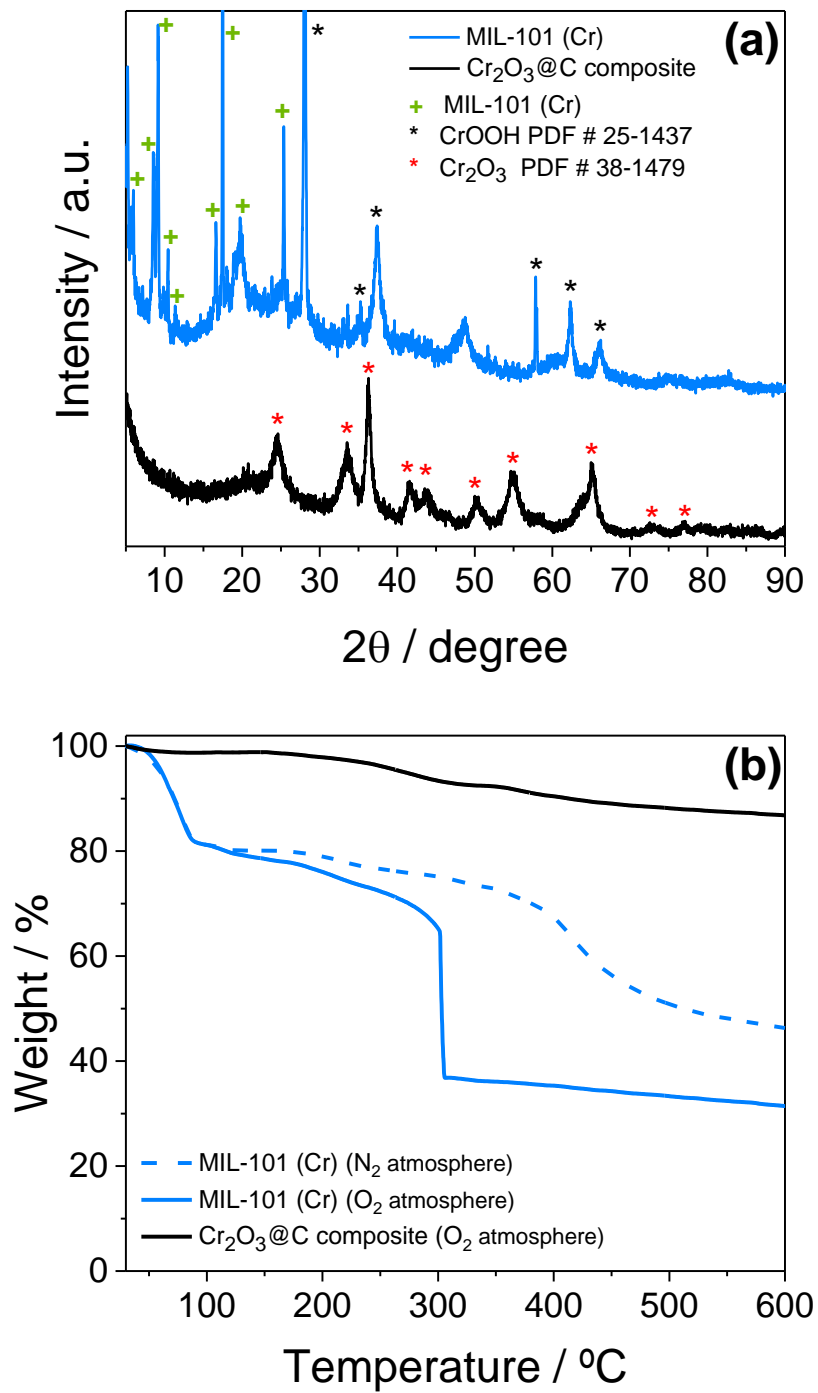


Figure 1

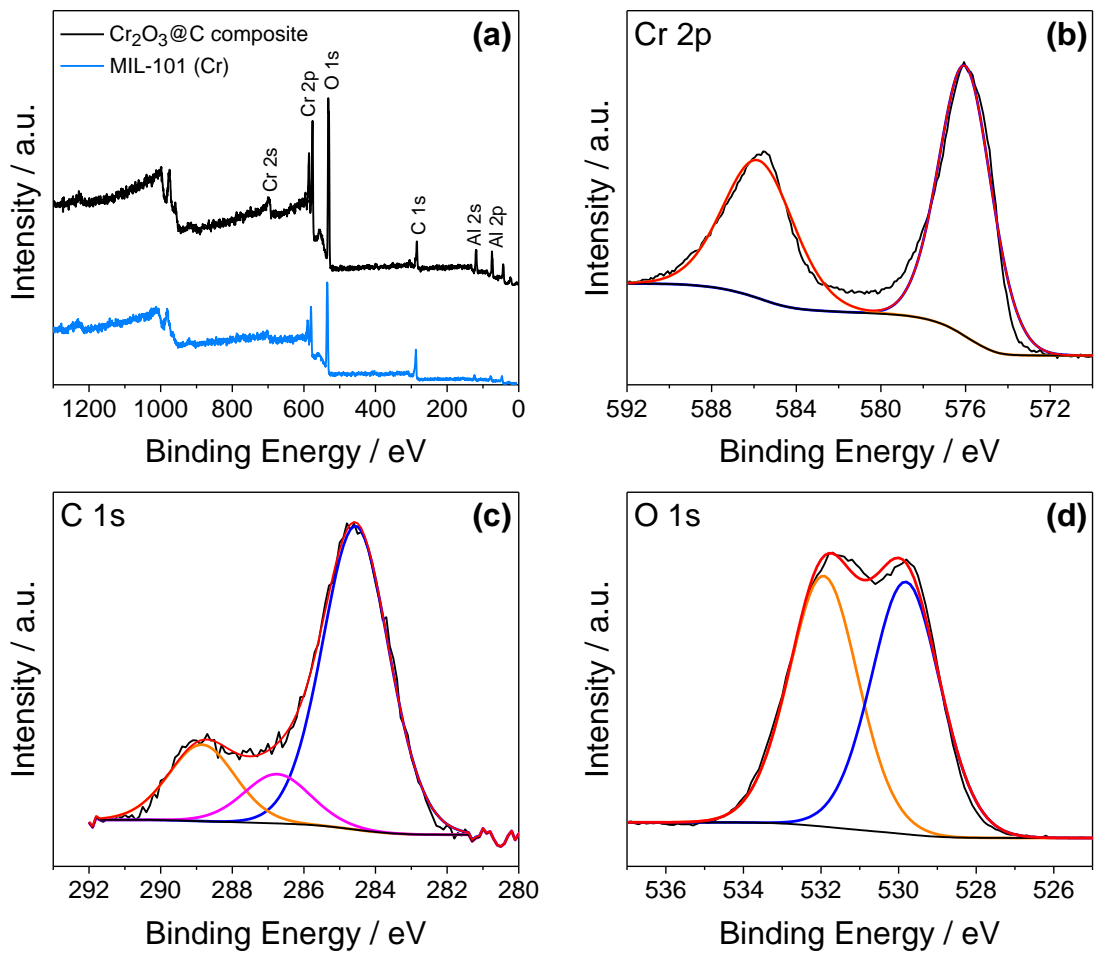


Figure 2

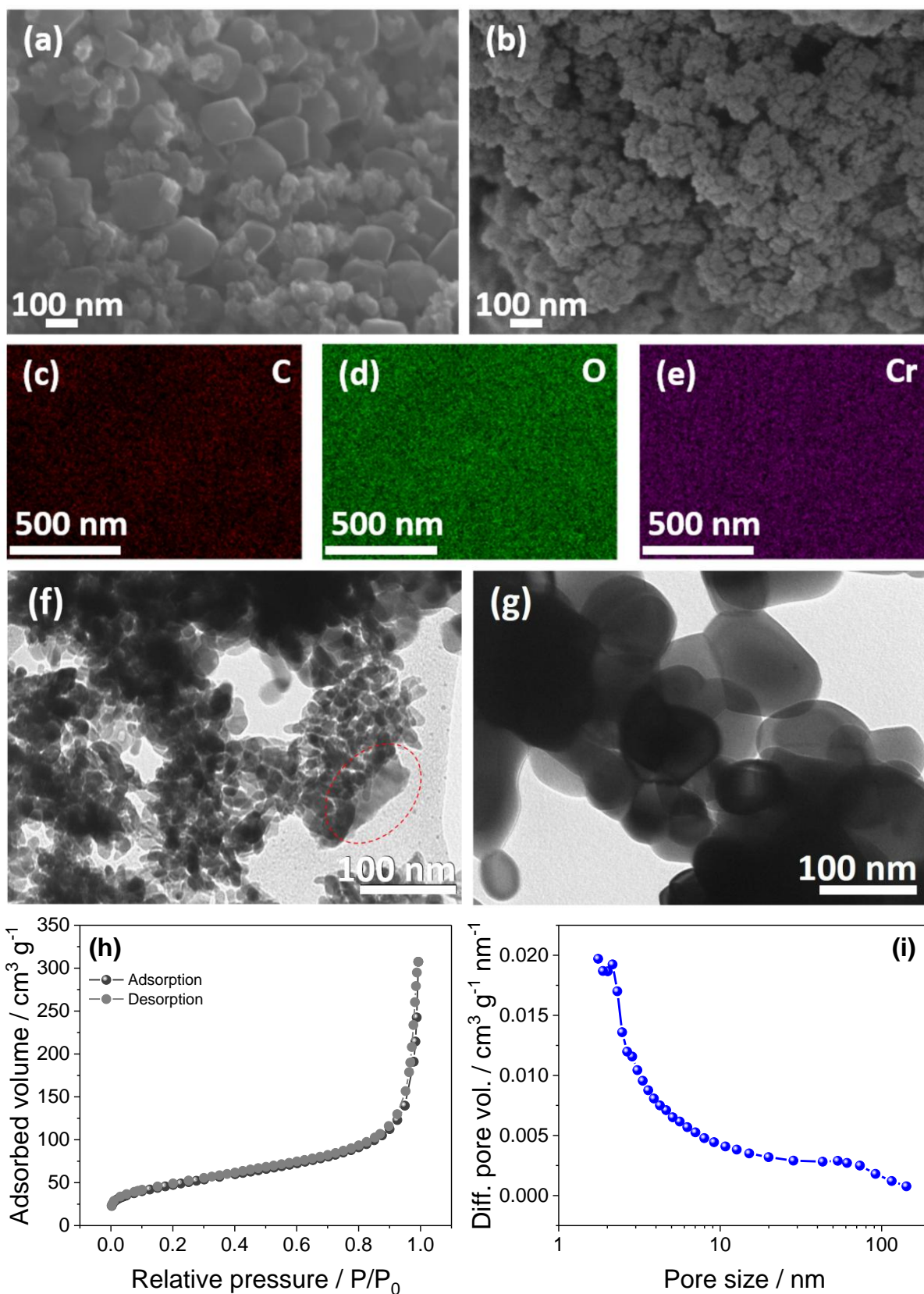


Figure 3

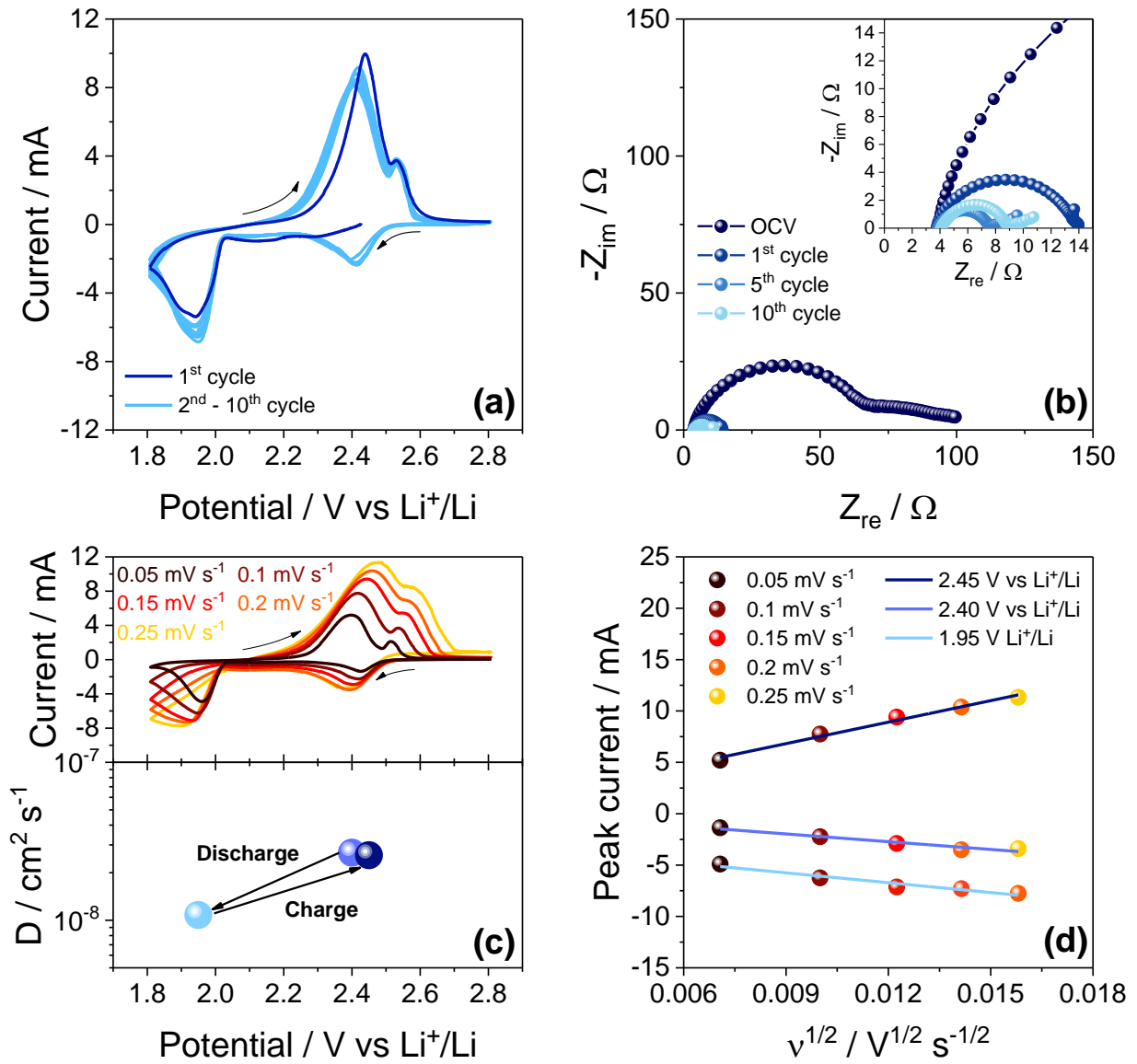


Figure 4

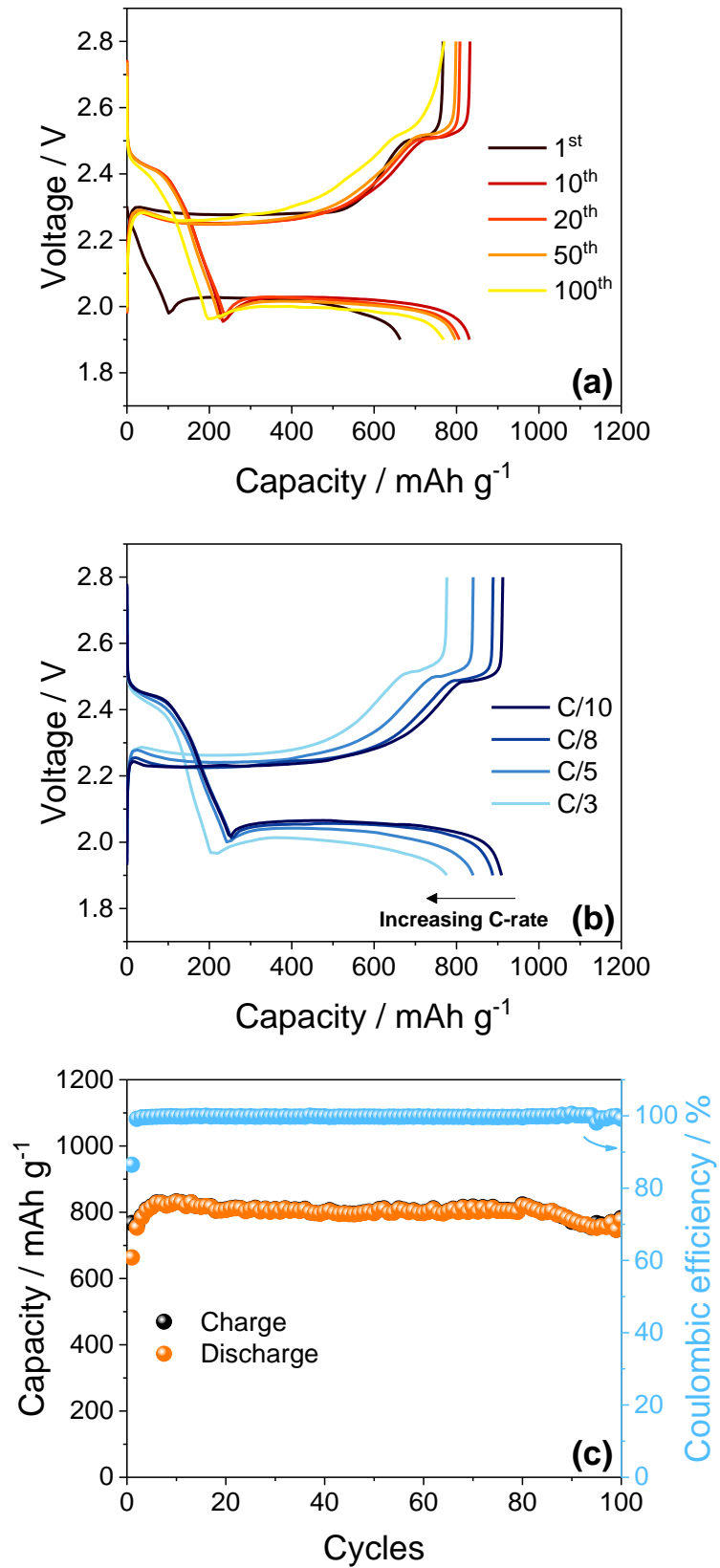


Figure 5

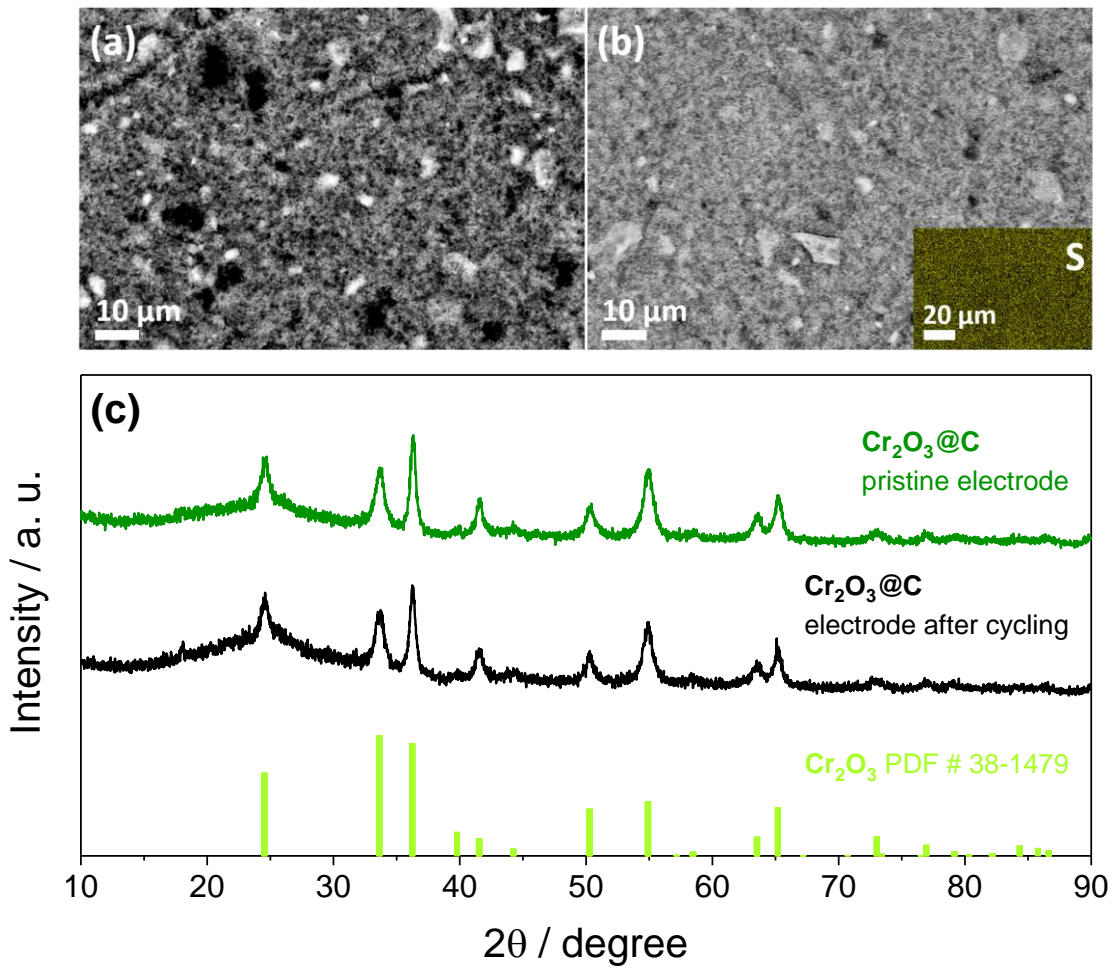


Figure 6

Porous Cr₂O₃@C composite derived from metal organic framework in efficient semi-liquid lithium-sulfur battery

Almudena Benitez¹, Vittorio Marangon², Celia Hernández-Rentero¹, Álvaro Caballero¹,

Julián Morales^{1*} and Jusef Hassoun^{2*}

¹ Dpto. Química Inorgánica e Ingeniería Química, Instituto de Química Fina y Nanoquímica, Universidad de Córdoba, 14071, Córdoba, Spain

² Department of Chemical and Pharmaceutical Sciences, University of Ferrara, Via Fossato di Mortara 17, Ferrara 44121, Italy

*Corresponding Authors: iq1mopaj@uco.es, jusef.hassoun@unife.it

Abstract

A carbon composite including Cr₂O₃ (Cr₂O₃@C) and benefitting of a metal organic framework (MOF) precursor is herein synthesized, and originally employed in a semi-liquid lithium-sulfur cell using a catholyte solution formed by Li₂S₈ polysulfide, conducting lithium salt and film forming additive dissolved in diethylene glycol dimethyl ether (DEGDME). The adopted cell configuration may actually allow the porous structure of the MOF derivative to efficiently enable the lithium/sulfur electrochemical process. Thus, structure, chemical composition, morphology and porosity of the composite are investigated by X-ray diffraction, X-ray photoelectron spectroscopy, scanning electron microscopy, and N₂ adsorption/desorption isotherms, respectively. The data reveal a mesoporous material consisting of aggregated nanometric particles (<100 nm) with relatively high BET surface area (170 m² g⁻¹), uniform element distribution, and a carbon content of about 13 wt.%. Cyclic voltammetry of the Cr₂O₃@C in semi-liquid lithium sulfur cell using the catholyte solution shows a reversible reaction with fast kinetics and Li-diffusion coefficient ranging from about 3×10⁻⁸ cm² s⁻¹ at 2.4 V vs. Li/Li⁺, to 1×10⁻⁸ cm² s⁻¹ at 2 V vs. Li/Li⁺. Furthermore, electrochemical impedance spectroscopy reveals a very stable interphase with an impedance below 5 Ω after an activation process promoted by cycling. The semi-liquid Li/S cell operates with remarkable stability and efficiency approaching 100%, delivers a capacity ranging from 900 mAh g⁻¹

¹ at C/10 rate to 780 mAh g⁻¹ at C/3 rate, and performs over 100 charge/discharge cycles with very modest capacity decay.

Keywords: MOF; Cr₂O₃; carbon composite; catholyte; semi-liquid Li/S battery

Introduction

A proper energy policy can drive the modern society for actually improving the life quality. On the other hand, an energy demand principally based on fossil fuels may lead to pollution, excessive emission of greenhouse gasses, and severe environmental challenges affecting health and climate [1,2]. In this view, an efficient and possibly low-cost energy storage is expected to allow the large scale use of environmentally compatible, while discontinuous, renewable energies such as wind and solar, further improve information and communication technologies, and promote the large scale diffusion of “green” applications such as electric vehicles (EVs) [3]. Lithium-ion battery (LIB), one of the most attracting electrochemical energy storage systems, has well promoted during the last decades the worldwide diffusion of portable electronics, smartphones and laptops [3–6]. In its most typical configuration, the LIB is based on insertion or intercalation electrodes such as graphite at the anode and layered transition metal oxide at the cathode, and has energy density ranging from 180 to 250 Wh kg⁻¹ with remarkable number of charge/discharge cycles [3]. The need for increased energy density to fully match the requirements of emergent applications (e.g., for extending the driving range of EVs) and the raise of issues ascribed to the relevant cost and possible toxicity of transition metals such as Co, triggered the research for alternative electrochemical energy storage systems [7,8]. Lithium sulfur (Li/S) battery presently appears as one of the most promising systems in terms of energy content and cycling ability [9], however with still intrinsic gap between fundamental research and practical application [10]. Indeed, Li/S cell has a theoretical specific capacity of 1675 mAh g⁻¹, that is, about one order of magnitude greater than that of common intercalation materials used in LIBs, and a theoretical energy density as high as 2500 Wh kg⁻¹ [11]. Furthermore, sulfur is characterized by a remarkable abundance, relevant environmental compatibility and low cost [12].

These very attracting characteristics may be jeopardized by the low electronic conductivity of sulfur, which has an insulating character, and by the solubility of the Li/S reaction products, that is, the lithium polysulfides, which can shuttle from the cathode to the anode and cause loss of active material and severe limitation of cell efficiency and cycle life [13]. Several strategies, including the use of various carbons [14,15], conductive polymers [16,17], metal oxides [18,19] and nanometric metals [20] into the electrode formulation have been proposed to mitigate these shortcomings.

Polypyrrol (PPy)@MnO₂@S with dual core-shell structure exploited the polar MnO₂ hollow spheres to provide inner space for alleviating the volume expansion for sulfur, and to effectively moderate the dissolution of polysulfides by synergistic effect of structural restriction and chemical adsorption, and generate sufficient electrical conduction. The Li/PPy@MnO₂@S cell delivered capacity ranging from about 1400 at 0.1C rate to about 700 mAh g⁻¹ at 1C rate and a capacity decay rate of 0.048% at 0.5C over 500 cycles [21]. Furthermore, MnO₂/GO/CNTs-S composite with three-dimensional architecture was synthesized by a one-pot chemical method and heat treatment. The MnO₂/GO nanosheets anchored on the sidewalls of CNTs had a dual-efficient absorption capability for polysulfide intermediates. The electrode delivered in lithium cell capacity from 1500 mAh g⁻¹ at 0.05C rate to above 900 mAh g⁻¹ at 1C rate [22]. Recently, a bimetallic-organic-framework hosting sulfur nanoparticles exploited porous graphite and cobalt-nickel oxides (C/NiCo₂O₄) to physically and chemically entrap polysulfides, and for enabling electrode conductivity. The composite sulfur cathode delivered in lithium cell an initial specific capacity of about 970 mAh g⁻¹ at 0.5C and final capacity of about 670 mAh g⁻¹ over 500 cycles [23]. Various alternative methods with very promising results were furthermore adopted to prepare sulfur-carbon composites and achieve sulfur anchorage, including *in-situ* deposition at the interspaces between carbon nanoparticles in aqueous solution at room temperature [24], template/casting for achieving flexible and free-standing carbon film using CNTs and graphene [25], clustering in a pomegranate-like structure [26], iron/nitrogen co-doping of graphene [27], and nitrogen-doping of graphene/titanium nitride nanowires [28]. All these synthesis procedures were

devoted to control the complex reaction of the sulfur in lithium cell which unavoidably involves dissolution and re-precipitation of polysulfides and sulfur over the electrodes with various morphological changes, as clearly indicated by a recent study of the reversible conversion of a sulfur–metal nanocomposite combining X-ray computed tomography at the micro- and nanoscales and electrochemistry [29]. Metal organic frameworks (MOFs) with micro- and meso-porosity have been suggested to confine the S particles and efficiently trap polysulfides [30]. Since the first report on the application of these compounds in Li/S batteries, in particular the MIL-100 (Cr) [31], new contributions aimed to improve their performances. In particular, particle size [32], nature of the metallic element and ligand [33,34], and coating with polymers [35] have been considered the most relevant factors for determining the MOFs characteristics in Li/S battery. However, a partially insulating nature and H₂O molecules connected to their framework by different types of bonds have led to a significant drop during cycling and limited the S content in the composite [36,37]. Recently, MOF/S composites with higher conductivity and improved performances have been achieved by using conductive additives such as reduced graphene oxide (rGO) [33,38], graphene nanosheets (GNS) [39], carbon nanotubes (CNT) [40] and conductive polymers, including poly (3,4-ethylenedioxythiophene) polystyrene sulfonate (PEDOT-PSS) [35] and polypyrrol (ppy) [41]. Another approach for enhancing the electrode conductivity, and promoting at the same time the interaction of the electrode host matrix with the polysulfides produced by Li/S reaction, consisted of the use carbon-metal oxide composites obtained from MOFs [30,37,42].

Herein, we extend the latter approach by using a carbon-chromium oxide MOF-derivative in a semi-liquid lithium-sulfur cell [43,44] exploiting the catholyte concept [45]. Composites including Cr₂O₃ and carbon, obtained by different procedures, have been principally used in Li-ion batteries. Indeed, Cr₂O₃/C electrodes have been efficiently used as Li-ion battery anode with enhanced cycling and rate performance compared with pure Cr₂O₃ due to the important role played by the carbon in improving the electrical conductivity of Cr₂O₃, inhibiting the aggregation and acting as a favourable buffer to the volume change during the electrochemical process [46,47]. Furthermore,

various cell using the semi-liquid, lithium-sulfur configuration have been reported and efficiently cycled by exploiting polysulfide containing solutions, indicated so far as *catholyte*. Three-dimensional reduced graphene oxide (3D-rGO) sponge allowed the efficient cycling of a Li_2S_6 catholyte with a capacity of about 1600 mAh g^{-1} at 0.1C, areal capacity of 3.5 mAh cm^{-2} and 98% coulombic efficiency over 200 cycles [48]. A cell exploiting sulfur/meso carbon micro beads (MCMB) electrode and Li_2S_8 containing catholyte efficiently operated by delivering a specific capacity approaching 1500 mAh g^{-1} for over 80 cycles at a C/5 rate, without significant capacity decay and with high coulombic efficiency [49]. A Li_2S_9 solution has also been used as catholyte in semi-liquid lithium-sulfur cell by using a porous carbon electrode as the current collector with a capacity approaching 600 mAh g^{-1} for about 70 cycles [50]. Furthermore, polysulfide has been included in solid membranes and used in a Li/S cell with capacity of about 1200, 1100, and 1000 mAh g^{-1} , respectively, at C/10, C/5, and C/3, however with a significant decay during cycling [51]. Lithium polysulfide has been employed in a flow battery design with embedded current collector networks exhibiting an electrochemical activity distributed throughout the volume of flow electrodes rather than being confined to surfaces of stationary current collectors. The nanoscale network architecture enabled cycling of a polysulfide solutions deep into precipitation regimes at C/4 rate, with an initial capacity of 1200 mAh g^{-1} and a capacity retention of 50% over 100 cycles [52]. These semi-liquid systems based on catholyte have mainly employed a carbon material as the support for the electrochemical process, while the combination of Cr_2O_3 and carbon has never been exploited in a semi-liquid Li/S cell according to the best of our knowledge. Nevertheless, Cr_2O_3 decorating carbon nanofibers were employed as coating in a multifunctional separator for high-performance Li-S batteries using a Li_2S_6 catholyte solution [53].

Therefore, the cell formed in our work by combining the carbon-chromium oxide MOF-derivative ($\text{Cr}_2\text{O}_3@\text{C}$) and the Li_2S_8 catholyte is expected to allow a reversible conversion into lithium and sulfur of Li_2S_8 active polysulfide, dissolved together with a lithium salt and a lithium-protecting additive into diethylene glycol dimethyl ether (DEGDME) [54]. This alternative cell configuration

is suggested as suitable approach to efficiently enable optimized performances of the MOF-derivative composites in Li/S battery.

Experimental Section

Preparation of MIL-101(Cr) and Cr₂O₃@C composite

The MIL-101(Cr) MOFs were prepared by a previously reported method [55,56]. Specifically, 2.0 g (5.0 mmol) of chromium (III) nitrate nonahydrate (Cr(NO₃)₃·9H₂O, Panreac) and 0.55 g (3.3 mmol) of 1,4-benzene dicarboxylic acid (H₂BDC, Sigma Aldrich) were dissolved in 50 mL of deionized water under vigorous stirring for 30 minutes to completely dissolve the dicarboxylic acid. The dark green suspension obtained was transferred to a 100 mL Teflon-lined autoclave. The mixture was sealed, held at 180 °C for 10 h and naturally cooled down to room temperature. Subsequently, MIL-101 was filtered, dipped into distilled water for one day, filtered again, washed several times with ethanol, and dried at 80 °C overnight. Then, as-synthesized MIL-101 was calcined in nitrogen atmosphere at 600 °C for 3 h in a tubular oven at a speed of 10 °C min⁻¹ using a constant gas flow of 50 mL min⁻¹ (preliminary purge was performed at room temperature for 30 min using N₂ flow of 100 mL min⁻¹). The final sample is subsequently indicated by the acronym Cr₂O₃@C.

Electrode preparation

The electrode was prepared by mixing 80 wt.% of Cr₂O₃@C, 10 wt.% of conductive agent (Super P carbon, Timcal) and 10 wt.% of polyvinylidene fluoride (PVDF 6020, Solvay) polymer binder in N-methyl-2-pyrrolidone (NMP, Sigma-Aldrich) to form a slurry. Then, a carbon paper (GDL, ELAT LT1400W, MTI Corp.) was used as substrate and coated with the slurry by doctor blade (MTI Corp.). The electrodes were dried in air for 3 hours at 70 °C by using a hot-plate to remove the solvent, cut into disks of 14-mm diameter, and vacuum dried overnight at 100 °C to remove residual traces of water and solvent before inserting in Ar-filled glovebox (MBraun, O₂ and H₂O content below 1 ppm).

Catholyte preparation

The catholyte was prepared inside Ar-filled glovebox (MBraun, O₂ and H₂O content below 1 ppm) according to our previous paper [54]. Elemental sulfur powder (Sigma-Aldrich) and lithium metal chopped (Rockwood Lithium) were mixed in a molar ratio of 4:1 and dissolved in diethylene glycol dimethyl ether (DEGDME, anhydrous, 99.5%, Sigma-Aldrich) with a final Li₂S₈ ratio of 5 wt.%. Then, the yellow suspension was heated at 80 °C overnight by stirring, and it turned dark red. To ensure the complete reaction between sulfur and lithium, the suspension was stirred for two more days without heating. The catholyte was obtained by adding to the latter solution lithium bis(trifluoromethanesulfonyl)imide (LiTFSI, Sigma-Aldrich) and lithium nitrate (LiNO₃, Sigma-Aldrich) with a ratio of 1 mole of each salt in ~~to~~ 1 kg of DEGDME solvent, and stirring for 12 h at room temperature. The catholyte used as a dissolved active material for the Li/S cell is subsequently indicated as DEGDME-Li₂S₈-1m LiNO₃-1m LiTFSI.

Materials Characterization

X-ray diffraction (XRD) patterns were obtained with a Bruker D8 Advance diffractometer using monochromatic Cu K α radiation. The patterns were recorded in the 2 θ range between 5° and 90° at a rate of 10 s per step with step size of 0.02°. Thermogravimetric analysis (TGA) was performed using a Mettler Toledo-TGA/DSC under nitrogen or oxygen atmosphere by heating the sample from 30 to 800 °C at 10 °C min⁻¹. X-ray photoelectron spectroscopy (XPS) measurements were carried out using a SPECS mod. PHOBIOS 150 MCD spectrometer using a Mg K α radiation and a chamber pressure able to reach 4 x 10⁻⁹ mbar. The textural properties were determined by a Micromeritics ASAP 2020 system using nitrogen as adsorbent. Pore size distribution was calculated by the Barret-Joyner-Halenda (BJH) method applied to the adsorption branch of the isotherms. Sample morphologies were investigated by transmission electron microscopy (TEM), employing a Zeiss EM 910 microscope equipped with a tungsten thermoionic electron gun operating at 100 kV, and through scanning electron microscopy (SEM) by means of a JEOL JSM-7800F for the

Cr₂O₃@C and precursor powders, and a Zeiss EVO 40 microscope equipped with a LaB₆ thermoionic electron gun for the Cr₂O₃@C electrode. The SEM was coupled to a microanalysis system for obtaining the energy dispersive X-ray spectra (EDS). SEM images of the Cr₂O₃@C electrode were also obtained at the pristine state and *ex-situ* after a galvanostatic cycling test performed at a constant current rate of C/5 (1C = 1675 mA g⁻¹) in lithium cell (see the next section for further details on the galvanostatic cycling conditions). Prior to the SEM analyses, the electrode was washed with dimethoxy ethane (DME) to remove possible traces of lithium salts, and subsequently dried under vacuum at room temperature for 20 minutes.

Cell assembly and electrochemical measurements

Electrochemical experiments were performed on CR2032 coin-type cells assembled inside an Ar-filled glove box (M-Braun, H₂O and O₂ content below 1 ppm). The cells were prepared by using the disk with 14 mm (1.4 cm) diameter coated by Cr₂O₃@C as the working electrode, a lithium metal disk as the counter/reference electrode and a polyethylene membrane (PE, Celgard) as the separator soaked by 80 μL of the catholyte solution, corresponding to a total sulfur loading of 4.4 mg. Taking into account the electrode geometric area (1.54 cm²) the sulfur surface loading was 2.9 mg cm⁻².

The electrochemical process was studied by cyclic voltammetry (CV) and electrochemical impedance spectroscopy (EIS) tests, which were carried out using a VersaSTAT MC Princeton Applied Research (PAR, AMETEK) analyzer. CV measurements were performed at a constant scan rate of 0.1 mV s⁻¹ within the 1.8–2.8 V range over ten cycles, as well as at scan rates increasing from 0.05 mV s⁻¹, to 0.1, 0.15, 0.2 and 0.25 mV s⁻¹ in order to determinate the lithium-ion diffusion coefficients (D_{Li}). EIS measurements were taken at the OCV, after the first, fifth, and tenth CV cycles in the 500 kHz–100 mHz frequency range using a 10 mV amplitude signal and the resulting Nyquist plots were studied by nonlinear least-squared (NLLSQ) fitting through a Boukamp tool [57]. It is worth mentioning that only fits with a χ^2 of the order of 10⁻⁴ or lower were considered suitable. Galvanostatic cycling tests were carried out within the 1.9–2.8 V range with a MACCOR

series 4000 battery test system using C-rates of C/10, C/8, C/5, and C /3 (1C=1675 mA g⁻¹). Both specific capacity and current rate were referred to the sulfur mass in the catholyte (4.4 mg in the coin cell). The narrower voltage range employed in the galvanostatic cycling tests was chosen in order to limit the formation of short-chain polysulfides, such as Li₂S, which occurs at lower voltage values and can lead to poor performances and short cycle life of the lithium-sulfur cell [13]. Instead, voltammetry has explored a more extended potential range in order to fully characterize the electrochemical process of the semi-liquid sulfur cell using the Cr₂O₃@C composite.

Results and discussion

The changes upon annealing of MIL-101(Cr) precursor to obtain the Cr₂O₃@C composite are detected by XRD and TGA in Figure 1. The XRD pattern of MIL-101(Cr) shown in Fig. 1a reveals the characteristic peaks below 25° of 2θ [31,58]. Above this value, intense peaks not assigned to the MIL-101(Cr) compound are also detected and ascribed to the α-CrOOH phase, thus suggesting the presence in the pristine MOF of a Cr oxy-hydroxide impurity [58]. After heating at 600 °C under N₂ only peaks belonging to the α-Cr₂O₃ phase are detected, while the typical peak of C assigned to (002) planes is not detected at 26.5° of 2θ, thus indicating its amorphous nature ascribed to a mild calcination temperature [59]. The TGA curves of the pristine MOF recorded under N₂ and O₂ atmosphere, respectively, as well as the curve of the Cr₂O₃@C recorded under O₂ atmosphere are shown in Fig. 1b. The TGA curves of MOF under N₂ and O₂ reveal similar weight loss of about 20% below 100 °C, which may be likely ascribed to the loss of physically adsorbed water. The observed weight loss is of about 8 H₂O (molecules per formula unit) higher than that reported by literature for MOFs with the same chemical composition, that is, Cr₃O(OH)(H₂O)₂(BDC)₃ [60]. On the other hand, an amount of adsorbed water as high as 40 % have been already reported in literature [61]. At temperatures higher than 100 °C the weight loss becomes greater in the O₂ atmosphere, being very pronounced around 300 °C where the expected oxidation of the organic matrix occurs. The total weight loss for the MOF precursor is therefore detected at 600 °C to be of about 70% [61]. Considering the theoretical MOF composition, including absorbed water, the

theoretical weight loss should be 68.3 % [60]: the difference with respect to our results (70 %) may be reasonably attributed to the presence of the above mentioned α -CrOOH impurity. The TGA curve recorded under N_2 reveals different kinetics and a lower overall weight loss, that is, of about 57 %, as expected by the missing oxidation of the organic matrix. On the other hand, the TGA curve recorded under O_2 of the $Cr_2O_3@C$ is characterized by weight loss only ascribed to CO_2 evolution, thus indicating a carbon content of about 13 % into the composite. The carbon content observed for the composite is lower than that expected by annealing the MIL-101(Cr) MOF [61], most likely due to a partial volatilization of the organic component during the thermal treatment and to the presence of α -CrOOH impurity in the pristine MOF.

Figure 1

The surface composition of the $Cr_2O_3@C$ composite is analyzed by XPS (Figure 2). The survey spectrum (Fig. 2a) clearly indicates the presence of Cr, C and O elements, along with Al used as the support for measurement. The spectrum of Cr 2p (Fig. 2b) may be resolved into peaks with binding energy values around 576.7 and 686.3 eV assigned to Cr 2p_{3/2} and Cr 2p_{1/2}, respectively, which suggests Cr³⁺ bound to O [62]. Furthermore, the C 1s spectrum (Fig. 2c) can be fitted according to three components located at 284.55 (70.7 %), 286.7 (11.5 %) and 288.9 (17.8 %) eV, assigned to C-C/C=C, C-O epoxy and C-O carboxyl environments, respectively [63]. Finally, the O 1s signal is fitted according to two components at 529.8 and 531.9 eV (Fig. 2d), where the first one is assigned to O²⁻ ions, while the second peak is more complex since it can be assigned to OH⁻ ions or to O⁻ ions, which can compensate deficiencies in the sub-surface of the transition metal oxide [64], and even to adsorbed H₂O [65]. The atomic concentrations calculated by XPS are 23.0, 62.4 and 15.6% for C, O and Cr, respectively. The XPS data indicate relevantly higher amount of O compared to the value estimated by the TGA curves of $Cr_2O_3@C$, thus suggesting a different surface composition for the sample with respect to the bulk as the XPS mainly focuses at the material surface.

Figure 2

Figure 3 reports the morphology of the composite as detected by SEM, EDS and TEM, as well as its textural properties determined by N₂ adsorption/desorption isotherms. The SEM image of the MOF precursor reported for comparison in Fig. 3a reveals particles having the typical pseudo-octahedral morphology of MIL-101(Cr) with size ranging between 100 nm and 200 nm, in addition to other particles characterized by a more irregular morphology most likely ascribed to the α -CrOOH [58]. In spite, the SEM of the Cr₂O₃@C composite (Fig. 3b) shows a morphology changes after calcination: the pseudo-octahedral morphology almost vanishes by pyrolysis of the organic ligand, being replaced by nanometric particles forming agglomerates (> 100 nm) with remarkably higher surface roughness, and very regular shape compared to the pristine MOF. In addition, the EDS elemental mapping reveals homogeneous C, O, and Cr elements distribution over the Cr₂O₃@C sample (Fig. 3c, d and e, respectively). The TEM images of the Cr₂O₃@C composite (Fig. 3f, g) well support the SEM data (compare with Fig. 3a, b), and show a wide size distribution of agglomerated particles ranging from few nanometers (Fig. 3f) to values approaching 100 nm (Fig. 3g). It is worth mentioning that particle interconnection may be actually promoted by the carbon, which is detected by TGA in Fig. 1b to reach 13% in weight and most likely represented by light grey particles with an irregular shape, such that circled in the TEM image of fig. 3f. The surface area and pore volume of the Cr₂O₃@C composite are determined by N₂ adsorption measurements (Fig 3h, i). The adsorption/desorption isotherm reported in Fig. 3h shows a hysteresis loop at high relative pressure indicating a narrow pore size distribution into the composite, and allows to calculate a BET surface area of 170 m² g⁻¹ and a pore volume of 0.5 cm³ g⁻¹. The pore size distribution (Fig. 3i) mainly indicates a mesoporous structure and an average pore size of 12 nm. It is worth noting that the shape of the isotherms and the specific surface values are in line with those reported for Cr₂O₃@C composites derived from MIL-101(Cr) MOF [66,67]. These values are expected to support an efficient reaction of the dissolved polysulfide in the semi-liquid Li/S cell [54]. Polysulfide-trapping ability of transition metal oxides included in the composition of the cathode support has been indicated in various papers to depend on the anchoring ability of the polar

sites of the oxide, which attract the sulfur and lead to the absorption of dissolved polysulfides [68–71]. In particular, the absorption ability of Cr_2O_3 has been recently demonstrated using nanoparticle decorating carbon fibers derived from solid leather wastes adopted as coating for separator and aimed to achieve high performance lithium-sulfur battery [53]. The absorbent properties of acetylene black (AB) and Cr_2O_3 were measured in the above work using a Li_2S_6 polysulfide solution. Accordingly, polysulfide solutions exposed to AB upgraded by Cr_2O_3 powders turned nearly colorless and transparent, while the bare AB powders had a negligible impact on the color of the solution, thus qualitatively suggesting the polysulfide-trapping ability of the Cr_2O_3 .

Figure 3

Figure 4 reveals the electrochemical features of the $\text{Cr}_2\text{O}_3@\text{C}$ in a lithium cell employing the DEGDME- Li_2S_8 -1m LiNO_3 -1m LiTFSI catholyte [54]. The CV profiles recorded within 1.8-2.8 V at a constant scan rate of 0.1 mV s^{-1} (Fig. 4a) show during the first cathodic scan only one peak below 2 V ascribed to the reduction of Li_2S_8 to short chain polysulfides (e.g., Li_2S_4 , Li_2S_2), while the subsequent anodic scan reveals two defined peaks above 2.4 V ascribed to the oxidation of the short chain polysulfides back to Li_2S_8 and finally to S [54]. The subsequent cycles evidence voltammetry profiles characterized by two reduction peaks around 2 V and 2.4 V during cathodic scan, and two corresponding oxidation peaks above 2.4 V during anodic scan, ascribed to the reversible redox process of S and Li with formation of long- and short-chain polysulfides [72]. Furthermore, the voltage profiles well overlap and the polarization decreases, thus suggesting an optimized electrochemical process, the reversibility of which improves by the ongoing of cycles [54,72]. The electrode/electrolyte interphase evolution of the Li/DEGDME- Li_2S_8 -1m LiNO_3 -1m LiTFSI/ $\text{Cr}_2\text{O}_3@\text{C}$ cell upon voltammetry is detected by EIS upon cycling (Fig. 4b), and the recorded spectra are analysed by NLLSQ fitting (see Experimental section) [57]. The Nyquist plot of the cell in its pristine condition at the open circuit (OCV) can be represented by the $R_e(R_1Q_1)(R_2Q_2)$ equivalent circuit consisting of an electrolyte resistance (R_e) at high frequency values, a well-defined semicircle in the medium-high frequency region accounting for both the solid

electrolyte interphase (SEI) film formed at the electrodes surface and for the faradic charge-transfer (R_1Q_1), and a low-frequency depressed profile accounting for the lithium ion finite-length Warburg diffusion at the electrode/electrolyte interphase (R_2Q_2) [73,74]. After subsequent CV cycles the Nyquist plot shrinks, the impedance remarkably decreases while the profile modifies, particularly in the low-frequency region, being now represented by the new equivalent circuit $R_e(R_1Q_1)Q_2$ [75]. Hence, the depressed profile observed at the OCV at low-frequency modifies after CV cycles to form a tilted line associated with a semi-infinite Warburg element (Q_2) [75,76]. These changes are likely ascribed to the electrochemical activation of the electrode/electrolyte interphase upon the first cycle, and by the ongoing of the redox process which progressively promotes the reversible formation of sulfur and the various polysulfides at the $Cr_2O_3@C$ surface, as indeed observed for this kind of catholyte using a different electrode structure [54]. Accordingly, the electrode/electrolyte interphase resistance obtained from the semicircle width drops from about 60 Ω at OCV to values as low as 4.7 Ω after 10 cycles (see Table 1), which is in line with the CV profiles that suggest progressive improvement of the reactions kinetics by cycling.

Table 1

A further important characteristic of the electrode/electrolyte interphase is represented by the lithium-ion diffusion coefficient D_{Li} which may be obtained from CV measurements performed at various scan rates (Fig. 4c, top) and calculated at the different state of charge (Fig. 4c bottom) using the Randles-Sevcik equation [77–79]:

$$I_p = 2.69 \times 10^5 n^{3/2} A D_{Li}^{0.5} v^{0.5} C_{Li} \quad (1)$$

where I_p is the peak current, n is the number of electrons transferred during the reaction, A is the electrode geometric area, v the scanning rate, and C_{Li} the concentration of lithium ions in the catholyte. According to Eq. (1), D_{Li} may be determined by the slope of the linear plot of I_p vs $v^{0.5}$ both during cathodic and during anodic scans (Fig. 4d). Two peaks, at about 2.4 and 2 V, are considered for D_{Li} calculation during the cathodic scan, while only the major peak above 2.4 V is taken into account during anodic scan since the subsequent minor peak can generally merge into the

latter making problematic the evaluation [72]. Therefore, the values of D_{Li} determined taking into account the above mentioned peaks are of 2.7×10^{-8} , 1.1×10^{-8} , and 2.6×10^{-8} $\text{cm}^2 \text{s}^{-1}$, respectively. These values exceed the ones previously observed for the Li/S cell [72], most likely due to the nature of the cell involving an enhanced carbon/metal oxide substrate and a catholyte instead of a solid electrode.

Figure 4

Galvanostatic discharge–charge experiments were carried out to evaluate the performance of the $\text{Cr}_2\text{O}_3@\text{C}$ composite in the semi-liquid Li/S cell using the DEGDME-Li₂S₈-1m LiNO₃-1m LiTFSI catholyte at a current density of C/5 ($1\text{C} = 1675 \text{ mA g}^{-1}$) and at various C-rates (Figure 5). The voltage profiles of the cell at C/5 rate (Fig. 5a) show upon the first activation cycle (see discussion of CV in Fig 4a) the two discharge plateaus at about 2.4 and 2 V, corresponding to the reversible reaction of sulfur to form long and short chain polysulfides, respectively, which are reversed during charge into two plateaus at about 2.3 and 2.5 V in line with the CV curves. Furthermore, Fig. 5a indicates that the cell at the steady state can deliver reversibly and with relatively low polarization a specific capacity exceeding 800 mAh g^{-1} . Insights on the cell performances at various currents is given by the cycling profiles of Fig 5b which displays a steady state capacity approaching 900 mAh g^{-1} at C/10 and C/8, exceeding 800 mAh g^{-1} at C/5, and slightly below 800 mAh g^{-1} at C/3 rate. The decrease of the capacity by increasing the C-rate may be ascribed to the increase of the cell polarization by raising currents. Therefore, we can assume that the $\text{Cr}_2\text{O}_3@\text{C}$ composite enables efficient reaction of the semi-liquid lithium sulfur cell and a suitable polysulfides reversible conversion from C/10 to C/3 rate, with capacity ranging from 800 to 900 mAh g^{-1} , that is, a moderate range of operation in line with similar cell configuration [54,80]. Remarkably, the cell cycled at C/5 holds almost its steady state capacity of about 800 mAh g^{-1} with only limited signs of decay for 100 charge/discharge cycles, and retains a Coulombic efficiency approaching 100% over the whole cycling test (Fig. 5c).

Figure 5

The structural and morphological retention of the Cr₂O₃@C electrode is investigated in Figure 6 by *ex-situ* SEM/EDS and XRD analyses performed before and after cycling at C/5 rate (1C = 1675 mA g⁻¹). The SEM of the pristine electrode (Fig. 6a) shows that the heterogeneous morphology of the material remains almost unchanged upon cycling (Fig. 6b), while the brightness of the image intensifies as most likely due to the insulating character of traces of sulfur crystallized on the surface during the electrochemical process. This speculation is fully supported by the EDS elemental map reported in inset in Fig. 6b, which shows sulfur atoms uniformly distributed on the electrode surface after cycling. Furthermore, the structural stability of the material upon cycling is highlighted by the XRD analyses of Fig. 6c which evidence the retention of the α -Cr₂O₃ phase upon operating in Li/S cell, and the absence of undesired by-products formation, thus suggesting the inert nature of the Cr₂O₃@C composite. Therefore, these remarkable features, as well as the promising electrochemical performances, suggest the Cr₂O₃@C composite as a suitable electrode material for application in alternative Li/S cell configuration such as the semi-liquid one investigated in this work.

Figure 6

Conclusions

In summary, a composite Cr₂O₃@C has been synthesized from MIL-101(Cr) MOF, characterized by various chemical-physical techniques and successfully employed as the electrode support for the Li/S reaction in a **semi-liquid** cell employing a DEGDME-Li₂S₈-1m LiNO₃-1m LiTFSI catholyte. The composite revealed a morphology consisting of agglomerated mesoporous particles with a size below 100 nm, homogeneous C, O, and Cr elements distribution, a BET surface area as high as 170 m² g⁻¹ and a pore volume of 0.5 cm³ g⁻¹. Furthermore, the test revealed that the composite is predominantly formed by Cr₂O₃ **with a carbon weight ratio of about 13% due to the preparation technique which involved calcination in a nitrogen atmosphere at 600 °C and avoided oxidizing condition. On the other hand, bare Cr₂O₃ samples without carbon, not considered herein, may partially have semiconductor character, with a gap band of 3.3 eV [81], which is achieved both by**

oxidizing and reducing conditions as well as by doping with other oxides such as TiO_2 to create defects and increase the mobility of carriers [82]. The $\text{Cr}_2\text{O}_3@\text{C}$ material enabled the reversible Li_2S_8 conversion to short chain polysulfides and back to sulfur with efficient kinetics and potentials ranging from about 2 V to above 2.4 V vs. Li^+/Li . This performance was attributed to an enhanced electrode/electrolyte interphase characterized by resistance values below 5 Ω upon an electrochemical activation process, and a diffusion coefficient exceeding $10^{-8} \text{ cm}^2 \text{ s}^{-1}$ at the various states of the charge. The Li/S semi-liquid cell has operated between C/10 and C/3 current rate with a specific capacity ranging from about 900 mAh g^{-1} to values slightly below 800 mAh g^{-1} . Furthermore, the battery revealed remarkable stability, and a Coulombic efficiency approaching 100% at the steady state, while *ex-situ* SEM and XRD analyses evidenced the retention of both the electrode morphology and structure upon cycling. These findings well suggest the $\text{Cr}_2\text{O}_3@\text{C}$ composite as suitable electrode for application in the alternative, semi-liquid lithium sulfur cell configuration.

Acknowledgements

This work was funded by the grant “Fondo di Ateneo per la Ricerca Locale (FAR) 2019”, University of Ferrara, within the collaboration project “Accordo di Collaborazione Quadro 2015” between University of Ferrara (Chemical and Pharmaceutical Sciences Department) and Sapienza University of Rome (Chemistry Department). The research was also funded by Ministerio de Economía y Competitividad (Project MAT2017-87541-R) and Junta de Andalucía (Group FQM-175).

References

- [1] J. Chen, C. Li, Z. Ristovski, A. Milic, Y. Gu, M.S. Islam, et al., A review of biomass burning: Emissions and impacts on air quality, health and climate in China, *Sci. Total Environ.* 579 (2017) 1000–1034. doi:10.1016/j.scitotenv.2016.11.025.
- [2] C.D. Thomas, A. Cameron, R.E. Green, M. Bakkenes, L.J. Beaumont, Y.C. Collingham, et

- al., Extinction risk from climate change, *Nature*. 427 (2004) 145–148.
doi:10.1038/nature02121.
- [3] D. Di Lecce, R. Verrelli, J. Hassoun, Lithium-ion batteries for sustainable energy storage: Recent advances towards new cell configurations, *Green Chem.* 19 (2017) 3442–3467.
doi:10.1039/c7gc01328k.
- [4] B. Scrosati, Recent advances in lithium ion battery materials, *Electrochim. Acta.* 45 (2000) 2461–2466. doi:10.1016/S0013-4686(00)00333-9.
- [5] B. Scrosati, J. Hassoun, *Lithium batteries: Current technologies and future trends*, 2012.
doi:10.1533/9780857096371.4.573.
- [6] J.L. Sullivan, L. Gaines, Status of life cycle inventories for batteries, *Energy Convers. Manag.* 58 (2012) 134–148. doi:10.1016/j.enconman.2012.01.001.
- [7] A. Yoshino, Development of the Lithium-Ion Battery and Recent Technological Trends, in: G. Pistoia (Ed.), *Lithium-Ion Batter.*, Elsevier, 2014: pp. 1–20. doi:10.1016/B978-0-444-59513-3.00001-7.
- [8] J.B. Goodenough, Electrochemical energy storage in a sustainable modern society, *Energy Environ. Sci.* 7 (2014) 14–18. doi:10.1039/c3ee42613k.
- [9] L. Carbone, S.G. Greenbaum, J. Hassoun, Lithium sulfur and lithium oxygen batteries: new frontiers of sustainable energy storage, 1 (2017) 228–247. doi:10.1039/C6SE00124F.
- [10] R. Fang, S. Zhao, Z. Sun, D.-W. Wang, H.-M. Cheng, F. Li, More Reliable Lithium-Sulfur Batteries: Status, Solutions and Prospects, *Adv. Mater.* 29 (2017) 1606823.
doi:10.1002/adma.201606823.
- [11] J. Kim, D.-J. Lee, H.-G. Jung, Y.-K. Sun, J. Hassoun, B. Scrosati, An Advanced Lithium-Sulfur Battery, *Adv. Funct. Mater.* 23 (2013) 1076–1080. doi:10.1002/adfm.201200689.
- [12] L. Ma, K.E. Hendrickson, S. Wei, L.A. Archer, Nanomaterials: Science and applications in the lithium-sulfur battery, *Nano Today*. 10 (2015) 315–338.
doi:10.1016/j.nantod.2015.04.011.

- [13] C. Barchasz, J.C. Leprêtre, F. Alloin, S. Patoux, New insights into the limiting parameters of the Li/S rechargeable cell, *J. Power Sources*. 199 (2012) 322–330.
doi:10.1016/j.jpowsour.2011.07.021.
- [14] N. Moreno, A. Caballero, L. Hernán, J. Morales, J. Canales-Vázquez, Ordered mesoporous carbons obtained by a simple soft template method as sulfur immobilizers for lithium-sulfur cells, *Phys. Chem. Chem. Phys.* 16 (2014) 17332–17340. doi:10.1039/c4cp02829e.
- [15] R. Wu, S. Chen, J. Deng, X. Huang, Y. Song, R. Gan, et al., Hierarchically porous nitrogen-doped carbon as cathode for lithium–sulfur batteries, *J. Energy Chem.* 27 (2018) 1661–1667.
doi:10.1016/j.jechem.2018.02.010.
- [16] Y. Yang, G. Yu, J.J. Cha, H. Wu, M. Vosgueritchian, Y. Yao, et al., Improving the performance of lithium-sulfur batteries by conductive polymer coating, *ACS Nano*. 5 (2011) 9187–9193. doi:10.1021/nn203436j.
- [17] G. Ma, F. Huang, Z. Wen, Q. Wang, X. Hong, J. Jin, et al., Enhanced performance of lithium sulfur batteries with conductive polymer modified separators, *J. Mater. Chem. A*. 4 (2016) 16968–16974. doi:10.1039/C6TA07198H.
- [18] Z. Wei Seh, W. Li, J.J. Cha, G. Zheng, Y. Yang, M.T. McDowell, et al., Sulphur–TiO₂ yolk–shell nanoarchitecture with internal void space for long-cycle lithium–sulphur batteries, *Nat. Commun.* 4 (2013) 1331. doi:10.1038/ncomms2327.
- [19] F. Luna-Lama, C. Hernández-Rentero, A. Caballero, J. Morales, Biomass-derived carbon/ γ -MnO₂ nanorods/S composites prepared by facile procedures with improved performance for Li/S batteries, *Electrochim. Acta*. 292 (2018) 522–531. doi:10.1016/j.electacta.2018.09.176.
- [20] V. Marangon, J. Hassoun, Sulfur Loaded by Nanometric Tin as a New Electrode for High- Performance Lithium/Sulfur Batteries, *Energy Technol.* 7 (2019) 1900081.
doi:10.1002/ente.201900081.
- [21] Y. Li, B. Shi, W. Liu, R. Guo, H. Pei, D. Ye, et al., Hollow polypyrrole @ MnO₂ spheres as nano-sulfur hosts for improved lithium-sulfur batteries, *Electrochim. Acta*. 260 (2018) 912–

920. doi:10.1016/j.electacta.2017.12.068.

- [22] Y. Li, D. Ye, W. Liu, B. Shi, R. Guo, H. Zhao, et al., A MnO₂/Graphene Oxide/Multi-Walled Carbon Nanotubes-Sulfur Composite with Dual-Efficient Polysulfide Adsorption for Improving Lithium-Sulfur Batteries, *ACS Appl. Mater. Interfaces*. 8 (2016) 28566–28573. doi:10.1021/acsami.6b04270.
- [23] X. Zhang, Y. Fan, M.A. Khan, H. Zhao, D. Ye, J. Wang, et al., Co–Ni Binary- Metal Oxide Coated with Porous Carbon Derived from Metal- Organic Framework as Host of Nano- Sulfur for Lithium- Sulfur Batteries, *Batter. Supercaps*. 3 (2020) 108–116. doi:10.1002/batt.201900121.
- [24] Y.-S. Su, A. Manthiram, A facile in situ sulfur deposition route to obtain carbon-wrapped sulfur composite cathodes for lithium-sulfur batteries, *Electrochim. Acta*. 77 (2012) 272–278. doi:10.1016/j.electacta.2012.06.002.
- [25] M. Li, W. Wahyudi, P. Kumar, F. Wu, X. Yang, H. Li, et al., Scalable Approach To Construct Free-Standing and Flexible Carbon Networks for Lithium–Sulfur Battery, *ACS Appl. Mater. Interfaces*. 9 (2017) 8047–8054. doi:10.1021/acsami.6b12546.
- [26] W. Li, Z. Liang, Z. Lu, H. Yao, Z.W. Seh, K. Yan, et al., A Sulfur Cathode with Pomegranate-Like Cluster Structure, *Adv. Energy Mater*. 5 (2015). doi:10.1002/aenm.201500211.
- [27] L. Zhang, P. Liang, X.-L. Man, D. Wang, J. Huang, H.-B. Shu, et al., Fe, N co-doped graphene as a multi-functional anchor material for lithium-sulfur battery, *J. Phys. Chem. Solids*. 126 (2019) 280–286. doi:10.1016/j.jpcs.2018.11.027.
- [28] Z. Li, Q. He, X. Xu, Y. Zhao, X. Liu, C. Zhou, et al., A 3D Nitrogen-Doped Graphene/TiN Nanowires Composite as a Strong Polysulfide Anchor for Lithium–Sulfur Batteries with Enhanced Rate Performance and High Areal Capacity, *Adv. Mater*. 30 (2018). doi:10.1002/adma.201804089.
- [29] V. Marangon, D. Di Lecce, F. Orsatti, D.J.L. Brett, P.R. Shearing, J. Hassoun, Investigating

high-performance sulfur–metal nanocomposites for lithium batteries, *Sustain. Energy Fuels*. 4 (2020) 2907–2923. doi:10.1039/D0SE00134A.

- [30] S. Kuyuldar, D.T. Genna, C. Burda, On the potential for nanoscale metal–organic frameworks for energy applications, *J. Mater. Chem. A*. 7 (2019) 21545–21576. doi:10.1039/C9TA09896H.
- [31] R. Demir-Cakan, M. Morcrette, F. Nouar, C. Davoisne, T. Devic, D. Gonbeau, et al., Cathode Composites for Li–S Batteries via the Use of Oxygenated Porous Architectures, *J. Am. Chem. Soc.* 133 (2011) 16154–16160. doi:10.1021/ja2062659.
- [32] X.-J. Hong, T.-X. Tan, Y.-K. Guo, X.-Y. Tang, J.-Y. Wang, W. Qin, et al., Confinement of polysulfides within bi-functional metal–organic frameworks for high performance lithium–sulfur batteries, *Nanoscale*. 10 (2018) 2774–2780. doi:10.1039/C7NR07118C.
- [33] Y. Hou, H. Mao, L. Xu, MIL-100(V) and MIL-100(V)/rGO with various valence states of vanadium ions as sulfur cathode hosts for lithium-sulfur batteries, *Nano Res.* 10 (2017) 344–353. doi:10.1007/s12274-016-1326-0.
- [34] J. Zhou, R. Li, X. Fan, Y. Chen, R. Han, W. Li, et al., Rational design of a metal–organic framework host for sulfur storage in fast, long-cycle Li–S batteries, *Energy Environ. Sci.* 7 (2014) 2715. doi:10.1039/C4EE01382D.
- [35] W.-W. Jin, H.-J. Li, J.-Z. Zou, S.-Z. Zeng, Q.-D. Li, G.-Z. Xu, et al., Conducting polymer-coated MIL-101/S composite with scale-like shell structure for improving Li–S batteries, *RSC Adv.* 8 (2018) 4786–4793. doi:10.1039/C7RA12800B.
- [36] P.M. Shanthi, P.J. Hanumantha, B. Gattu, M. Sweeney, M.K. Datta, P.N. Kumta, Understanding the Origin of Irreversible Capacity loss in Non-Carbonized Carbonate – based Metal Organic Framework (MOF) Sulfur hosts for Lithium – Sulfur battery, *Electrochim. Acta*. 229 (2017) 208–218. doi:10.1016/j.electacta.2017.01.115.
- [37] Y. Zheng, S. Zheng, H. Xue, H. Pang, Metal–organic frameworks for lithium–sulfur batteries, *J. Mater. Chem. A*. 7 (2019) 3469–3491. doi:10.1039/C8TA11075A.

- [38] W. Bao, Z. Zhang, Y. Qu, C. Zhou, X. Wang, J. Li, Confine sulfur in mesoporous metal–organic framework @ reduced graphene oxide for lithium sulfur battery, *J. Alloys Compd.* 582 (2014) 334–340. doi:10.1016/j.jallcom.2013.08.056.
- [39] Z. Zhao, S. Wang, R. Liang, Z. Li, Z. Shi, G. Chen, Graphene-wrapped chromium–MOF(MIL-101)/sulfur composite for performance improvement of high-rate rechargeable Li–S batteries, *J. Mater. Chem. A.* 2 (2014) 13509–13512. doi:10.1039/C4TA01241K.
- [40] H. Zhang, W. Zhao, M. Zou, Y. Wang, Y. Chen, L. Xu, et al., 3D, Mutually Embedded MOF@Carbon Nanotube Hybrid Networks for High-Performance Lithium-Sulfur Batteries, *Adv. Energy Mater.* 8 (2018) 1800013. doi:10.1002/aenm.201800013.
- [41] H. Jiang, X.-C. Liu, Y. Wu, Y. Shu, X. Gong, F.-S. Ke, et al., Metal-Organic Frameworks for High Charge-Discharge Rates in Lithium-Sulfur Batteries, *Angew. Chemie Int. Ed.* 57 (2018) 3916–3921. doi:10.1002/anie.201712872.
- [42] Q. Wu, X. Zhou, J. Xu, F. Cao, C. Li, Carbon-based derivatives from metal-organic frameworks as cathode hosts for Li–S batteries, *J. Energy Chem.* 38 (2019) 94–113. doi:10.1016/j.jechem.2019.01.005.
- [43] Y. Yang, G. Zheng, Y. Cui, A membrane-free lithium/polysulfide semi-liquid battery for large-scale energy storage, *Energy Environ. Sci.* 6 (2013) 1552. doi:10.1039/c3ee00072a.
- [44] M. Agostini, D.-J.J. Lee, B. Scrosati, Y.K. Sun, J. Hassoun, Characteristics of Li₂S₈-tetraglyme catholyte in a semi-liquid lithium–sulfur battery, *J. Power Sources.* 265 (2014) 14–19. doi:10.1016/j.jpowsour.2014.04.074.
- [45] S. Phadke, E. Coadou, M. Anouti, Catholyte Formulations for High-Energy Li–S Batteries, *J. Phys. Chem. Lett.* 8 (2017) 5907–5914. doi:10.1021/acs.jpcllett.7b02936.
- [46] B. Guo, M. Chi, X.-G. Sun, S. Dai, Mesoporous carbon–Cr₂O₃ composite as an anode material for lithium ion batteries, *J. Power Sources.* 205 (2012) 495–499. doi:10.1016/j.jpowsour.2012.01.092.
- [47] Z. Cao, C. Zuo, Cr₂O₃/carbon nanosheet composite with enhanced performance for

- lithium ion batteries, *RSC Adv.* 7 (2017) 40243–40248. doi:10.1039/C7RA06188A.
- [48] P. Chiochan, S. Kosasang, N. Ma, S. Duangdangchote, P. Suktha, M. Sawangphruk, Confining Li₂S₆ catholyte in 3D graphene sponge with ultrahigh total pore volume and oxygen-containing groups for lithium-sulfur batteries, *Carbon N. Y.* 158 (2020) 244–255. doi:10.1016/j.carbon.2019.12.015.
- [49] D.J. Lee, M. Agostini, J.W. Park, Y.K. Sun, J. Hassoun, B. Scrosati, Progress in lithium-sulfur batteries: The effective role of a polysulfide-added electrolyte as buffer to prevent cathode dissolution, *ChemSusChem.* 6 (2013) 2245–2248. doi:10.1002/cssc.201300313.
- [50] S.S. Zhang, J.A. Read, A new direction for the performance improvement of rechargeable lithium/sulfur batteries, *J. Power Sources.* 200 (2012) 77–82. doi:10.1016/j.jpowsour.2011.10.076.
- [51] X. Yu, Z. Bi, F. Zhao, A. Manthiram, Hybrid Lithium–Sulfur Batteries with a Solid Electrolyte Membrane and Lithium Polysulfide Catholyte, *ACS Appl. Mater. Interfaces.* 7 (2015) 16625–16631. doi:10.1021/acsami.5b04209.
- [52] F.Y. Fan, W.H. Woodford, Z. Li, N. Baram, K.C. Smith, A. Helal, et al., Polysulfide Flow Batteries Enabled by Percolating Nanoscale Conductor Networks, *Nano Lett.* 14 (2014) 2210–2218. doi:10.1021/nl500740t.
- [53] Y. Guan, X. Liu, N. Akhtar, A. Wang, W. Wang, H. Zhang, et al., Cr₂O₃ Nanoparticle Decorated Carbon Nanofibers Derived from Solid Leather Wastes for High Performance Lithium-Sulfur Battery Separator Coating, *J. Electrochem. Soc.* 166 (2019) A1671–A1676. doi:10.1149/2.1181908jes.
- [54] D. Di Lecce, V. Marangon, A. Benítez, Á. Caballero, J. Morales, E. Rodríguez-Castellón, et al., High capacity semi-liquid lithium sulfur cells with enhanced reversibility for application in new-generation energy storage systems, *J. Power Sources.* 412 (2019) 575–585. doi:10.1016/j.jpowsour.2018.11.068.
- [55] W. Liu, J. Huang, Q. Yang, S. Wang, X. Sun, W. Zhang, et al., Multi-shelled Hollow Metal-

Organic Frameworks, *Angew. Chemie Int. Ed.* 56 (2017) 5512–5516.

doi:10.1002/anie.201701604.

- [56] J. Gu, X. Yin, X. Bo, L. Guo, High Performance Electrocatalyst Based on MIL-101(Cr)/Reduced Graphene Oxide Composite: Facile Synthesis and Electrochemical Detections, *ChemElectroChem*. 5 (2018) 2893–2901. doi:10.1002/celec.201800588.
- [57] B. BOUKAMP, A package for impedance/admittance data analysis, *Solid State Ionics*. 18–19 (1986) 136–140. doi:10.1016/0167-2738(86)90100-1.
- [58] H.M. Gobara, R.S. Mohamed, S.A. Hassan, F.H. Khalil, M.S. El-Sall, Pt and Ni Nanoparticles Anchored into Metal–Organic Frameworks MIL-101 (Cr) as Swift Catalysts for Ethanol Dehydration, *Catal. Letters*. 146 (2016) 1875–1885. doi:10.1007/s10562-016-1826-2.
- [59] F.J. Soler-Piña, C. Hernández-Rentero, A. Caballero, J. Morales, E. Rodríguez-Castellón, J. Canales-Vázquez, Highly graphitized carbon nanosheets with embedded Ni nanocrystals as anode for Li-ion batteries, *Nano Res.* 13 (2020) 86–94. doi:10.1007/s12274-019-2576-4.
- [60] S. Liu, F. Xu, L.-T. Liu, Y.-L. Zhou, W. Zhao, Heat capacities and thermodynamic properties of Cr-MIL-101, *J. Therm. Anal. Calorim.* 129 (2017) 509–514. doi:10.1007/s10973-017-6168-9.
- [61] M.-L. Chen, S.-Y. Zhou, Z. Xu, L. Ding, Y.-H. Cheng, Metal-Organic Frameworks of MIL-100(Fe, Cr) and MIL-101(Cr) for Aromatic Amines Adsorption from Aqueous Solutions, *Molecules*. 24 (2019) 3718. doi:10.3390/molecules24203718.
- [62] D. Briggs, *Handbook of X-ray Photoelectron Spectroscopy* C. D. Wanger, W. M. Riggs, L. E. Davis, J. F. Moulder and G. E. Muilenberg Perkin-Elmer Corp., Physical Electronics Division, Eden Prairie, Minnesota, USA, 1979. 190 pp. \$195, *Surf. Interface Anal.* 3 (1981) v–v. doi:10.1002/sia.740030412.
- [63] A. Benítez, A. Caballero, J. Morales, J. Hassoun, E. Rodríguez-Castellón, J. Canales-Vázquez, Physical activation of graphene: An effective, simple and clean procedure for

obtaining microporous graphene for high-performance Li/S batteries, *Nano Res.* 12 (2019) 759–766. doi:10.1007/s12274-019-2282-2.

- [64] J.-C. Dupin, D. Gonbeau, P. Vinatier, A. Levasseur, Systematic XPS studies of metal oxides, hydroxides and peroxides, *Phys. Chem. Chem. Phys.* 2 (2000) 1319–1324. doi:10.1039/a908800h.
- [65] J.R. Hoenigman, R.G. Keil, An XPS study of the adsorption of oxygen and water vapor on clean lithium films, *Appl. Surf. Sci.* 18 (1984) 207–222. doi:10.1016/0378-5963(84)90045-X.
- [66] Z. Wang, M. Li, Y. Ye, Y. Yang, Y. Lu, X. Ma, et al., MOF-derived binary mixed carbon/metal oxide porous materials for constructing simultaneous determination of hydroquinone and catechol sensor, *J. Solid State Electrochem.* 23 (2019) 81–89. doi:10.1007/s10008-018-4111-z.
- [67] A. Farisabadi, M. Moradi, S. Hajati, M.A. Kiani, J.P. Espinos, Controlled thermolysis of MIL-101(Fe, Cr) for synthesis of Fe_xO_y /porous carbon as negative electrode and Cr_2O_3 /porous carbon as positive electrode of supercapacitor, *Appl. Surf. Sci.* 469 (2019) 192–203. doi:10.1016/j.apsusc.2018.11.053.
- [68] X. Liu, J.-Q. Huang, Q. Zhang, L. Mai, Nanostructured Metal Oxides and Sulfides for Lithium-Sulfur Batteries, *Adv. Mater.* 29 (2017) 1601759. doi:10.1002/adma.201601759.
- [69] X. Tao, J. Wang, C. Liu, H. Wang, H. Yao, G. Zheng, et al., Balancing surface adsorption and diffusion of lithium-polysulfides on nonconductive oxides for lithium-sulfur battery design, 2016. doi:10.1038/ncomms11203.
- [70] X. Tao, J. Wang, Z. Ying, Q. Cai, G. Zheng, Y. Gan, et al., Strong Sulfur Binding with Conducting Magnéli-Phase $\text{Ti}_n\text{O}_{2n-1}$ Nanomaterials for Improving Lithium–Sulfur Batteries, *Nano Lett.* 14 (2014) 5288–5294. doi:10.1021/nl502331f.
- [71] X. Liang, C. Hart, Q. Pang, A. Garsuch, T. Weiss, L.F. Nazar, A highly efficient polysulfide mediator for lithium–sulfur batteries, *Nat. Commun.* 6 (2015) 5682.

[doi:10.1038/ncomms6682](https://doi.org/10.1038/ncomms6682).

- [72] L. Carbone, T. Coneglian, M. Gobet, S. Munoz, M. Devany, S. Greenbaum, et al., A simple approach for making a viable, safe, and high-performances lithium-sulfur battery, *J. Power Sources*. 377 (2018) 26–35. doi:10.1016/j.jpowsour.2017.11.079.
- [73] D.R. Franceschetti, J.R. Macdonald, R.P. Buck, Interpretation of finite-length-warburg-type impedances in supported and unsupported electrochemical cells with kinetically reversible electrodes, *J. Electrochem. Soc.* 138 (1991) 1368–1371. doi:10.1149/1.2085788.
- [74] L. Carbone, D. Di Lecce, M. Gobet, S. Munoz, M. Devany, S. Greenbaum, et al., Relevant Features of a Triethylene Glycol Dimethyl Ether-Based Electrolyte for Application in Lithium Battery, *ACS Appl. Mater. Interfaces*. 9 (2017) 17085–17095. doi:10.1021/acsami.7b03235.
- [75] T.Q. Nguyen, C. Breitkopf, Determination of Diffusion Coefficients Using Impedance Spectroscopy Data, *J. Electrochem. Soc.* 165 (2018) E826–E831. doi:10.1149/2.1151814jes.
- [76] D. Di Lecce, V. Gancitano, J. Hassoun, Investigation of Mn and Fe Substitution Effects on the Characteristics of High-Voltage $\text{LiCo}_{1-x}\text{M}_x\text{PO}_4$ ($x = 0.1, 0.4$) Cathodes Prepared by Sol–gel Route, *ACS Sustain. Chem. Eng.* 8 (2020) 278–289. doi:10.1021/acssuschemeng.9b05325.
- [77] J.E.B. Randles, A cathode ray polarograph. Part II.—The current-voltage curves, *Trans. Faraday Soc.* 44 (1948) 327–338. doi:10.1039/TF9484400327.
- [78] A. Ševčík, Oscillographic polarography with periodical triangular voltage, *Collect. Czechoslov. Chem. Commun.* 13 (1948) 349–377. doi:10.1135/cccc19480349.
- [79] D. Di Lecce, J. Hassoun, Lithium Transport Properties in $\text{LiMn}_{1-\alpha}\text{Fe}_\alpha\text{PO}_4$ Olivine Cathodes, *J. Phys. Chem. C*. 119 (2015) 20855–20863. doi:10.1021/acs.jpcc.5b06727.
- [80] S. Kim, H. Song, Y. Jeong, Flexible catholyte@carbon nanotube film electrode for high-performance lithium sulfur battery, *Carbon N. Y.* 113 (2017) 371–378. doi:10.1016/j.carbon.2016.11.019.

- [81] A. HOLT, P. KOFSTAD, Electrical conductivity and defect structure of Cr₂O₃. I. High temperatures (>~1000°C), Solid State Ionics. 69 (1994) 127–136. doi:10.1016/0167-2738(94)90401-4.
- [82] A. Holt, Electrical conductivity of Cr₂O₃ doped with TiO₂, Solid State Ionics. 117 (1999) 21–25. doi:10.1016/S0167-2738(98)00244-6.

List of tables

Table 1. NLLSQ analyses performed on the Nyquist plots reported in Fig. 4b. The impedance spectra were recorded by EIS upon CV, carried out on a Li/DEGDME-Li₂S₈-1m LiNO₃-1m LiTFSI/Cr₂O₃@C cell. See experimental section for samples' acronym.

List of figures

Figure 1. (a) X-ray diffraction (XRD) patterns of MIL-101 (Cr) MOF (cyan) and Cr₂O₃@C (black) composites; reference data of CrOOH (black stars, PDF # 25-1437) and Cr₂O₃ (red stars, PDF # 38-1479) are also reported for comparison. (b) Thermogravimetric analyses (TGA) curves of MIL-101 (Cr) MOF in N₂ and O₂ atmosphere (cyan) and Cr₂O₃@C in O₂ atmosphere (black). See experimental section for samples' acronym.

Figure 2. (a) X-ray photoelectron spectroscopy (XPS) survey spectra of MIL-101 (Cr) MOF (cyan) and Cr₂O₃@C (black) composites, and (b) Cr 2p, (c) C 1s and (d) O 1s deconvoluted XPS spectra of Cr₂O₃@C composite. See experimental section for samples' acronym.

Figure 3. (a,b) Scanning electron microscopy (SEM) images of MIL-101 (Cr) MOF (a) before and (b) after heating treatment, and (c-e) energy dispersion spectroscopy (EDS) elemental maps of Cr₂O₃@C composite. (f,g) Transmission electron microscopy (TEM) images of the Cr₂O₃@C powder; red circle in panel (f) highlights a carbon particle. (h) N₂ adsorption/desorption isotherms and (i) pore size distribution obtained through BJH method of Cr₂O₃@C composite. See experimental section for samples' acronym.

Figure 4. (a) Cyclic voltammetry (CV) measurement performed on a Li/DEGDME-Li₂S₈-1m LiNO₃-1m LiTFSI/Cr₂O₃@C cell at the constant scan rate of 0.1 mV s⁻¹ and (b) Nyquist plots recorded by electrochemical impedance spectroscopy (EIS) at the open circuit voltage (OCV) of the cell and after 1, 5 and 10 cycles (inset shows magnification). CV potential range: 1.8 – 2.8 V; EIS frequency range: 500 kHz – 100 mHz; EIS signal amplitude: 10 mV. (c) CV measurement performed on a Li/DEGDME-Li₂S₈-1m LiNO₃-1m LiTFSI/Cr₂O₃@C cell at various scan rates, that

is, 0.05, 0.1, 0.15, 0.2 and 0.25 mV s^{-1} (top panel) and corresponding lithium diffusion coefficients (D_{Li}) calculated through Randles-Sevcik equation (1) [77–79] (bottom panel). (d) Linear fitting of the peak currents obtained from the voltammograms reported in panel (c). CV potential range: 1.8 – 2.8 V. See experimental section for samples' acronym.

Figure 5. (a,b) Selected voltage profiles of the galvanostatic cycling measurement performed on a Li/DEGDME-Li₂S₈-1m LiNO₃-1m LiTFSI/Cr₂O₃@C cell (a) at the constant C-rate of C/5 (panel (c) shows the corresponding cycling trend and coulombic efficiency) and (b) at increasing C-rates, that is, C/10, C/8, C/5 and C/3 (1C = 1675 mA g⁻¹). Voltage range: 1.9 – 2.8 V. See experimental section for samples' acronym.

Figure 6. (a,b) Scanning electron microscopy (SEM) images of the Cr₂O₃@C electrode (a) at the pristine state and (b) after 7 cycles at C/5 (1C = 1675 mA g⁻¹) in a cell exploiting the Li/DEGDME-Li₂S₈-1m LiNO₃-1m LiTFSI/Cr₂O₃@C configuration. Voltage range: 1.9 – 2.8 V. Inset in panel (b) displays the corresponding energy dispersion spectroscopy (EDS) elemental map for sulfur. (c) X-ray diffraction (XRD) patterns of the Cr₂O₃@C electrode at the pristine state (dark green) and after the galvanostatic cycling test (black); reference data of Cr₂O₃ (light green, PDF # 38-1479) are also reported for comparison.

Cell condition	Circuit	R_1 [Ω]	χ^2
OCV	$R_e(R_1Q_1)(R_2Q_2)$	60 ± 2	2.7×10^{-4}
1 CV cycle	$R_e(R_1Q_1)$	10 ± 0.2	4.0×10^{-4}
5 CV cycles	$R_e(R_1Q_1)Q_2$	3.5 ± 0.1	1.5×10^{-4}
10 CV cycles	$R_e(R_1Q_1)Q_2$	4.7 ± 0.1	5.9×10^{-5}

Table 1

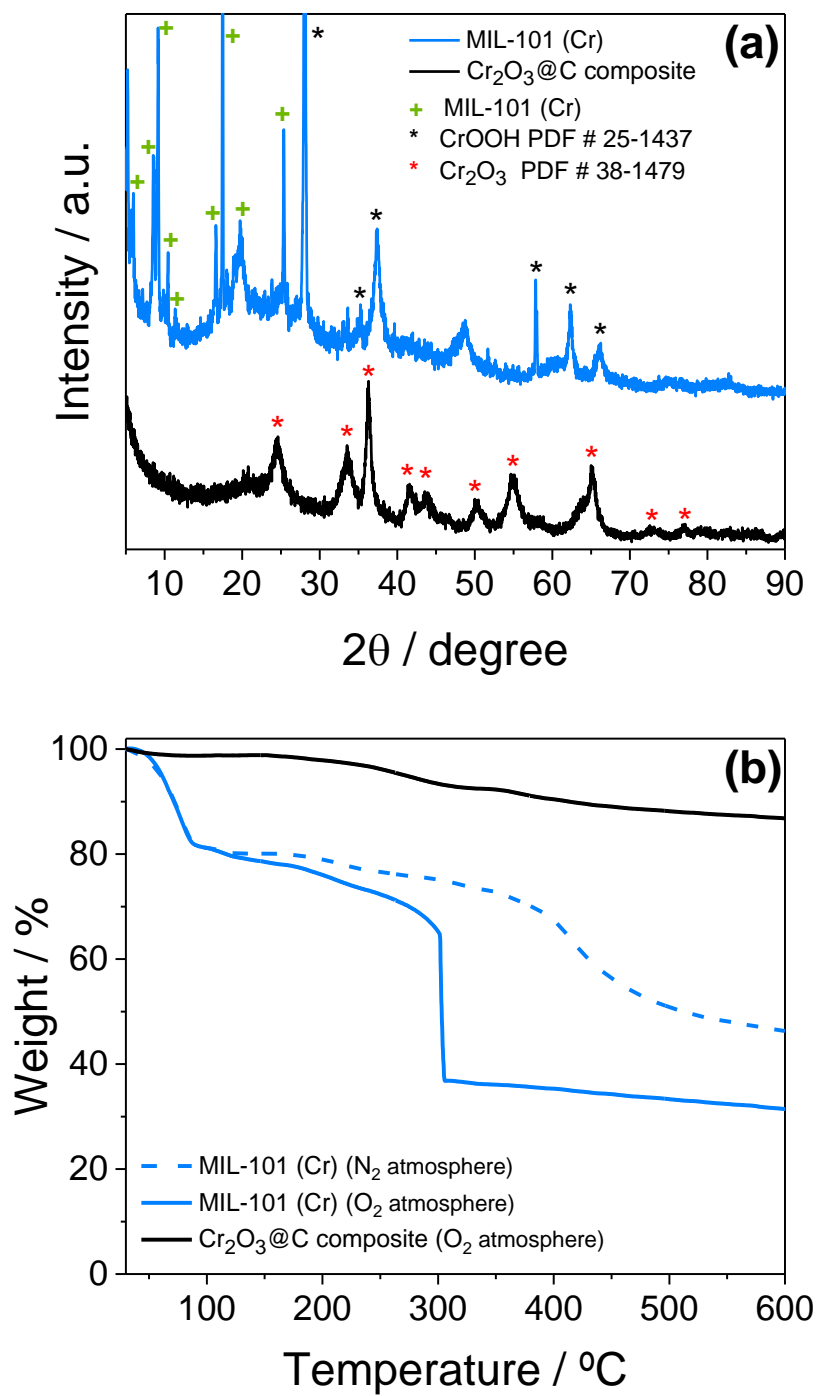


Figure 1

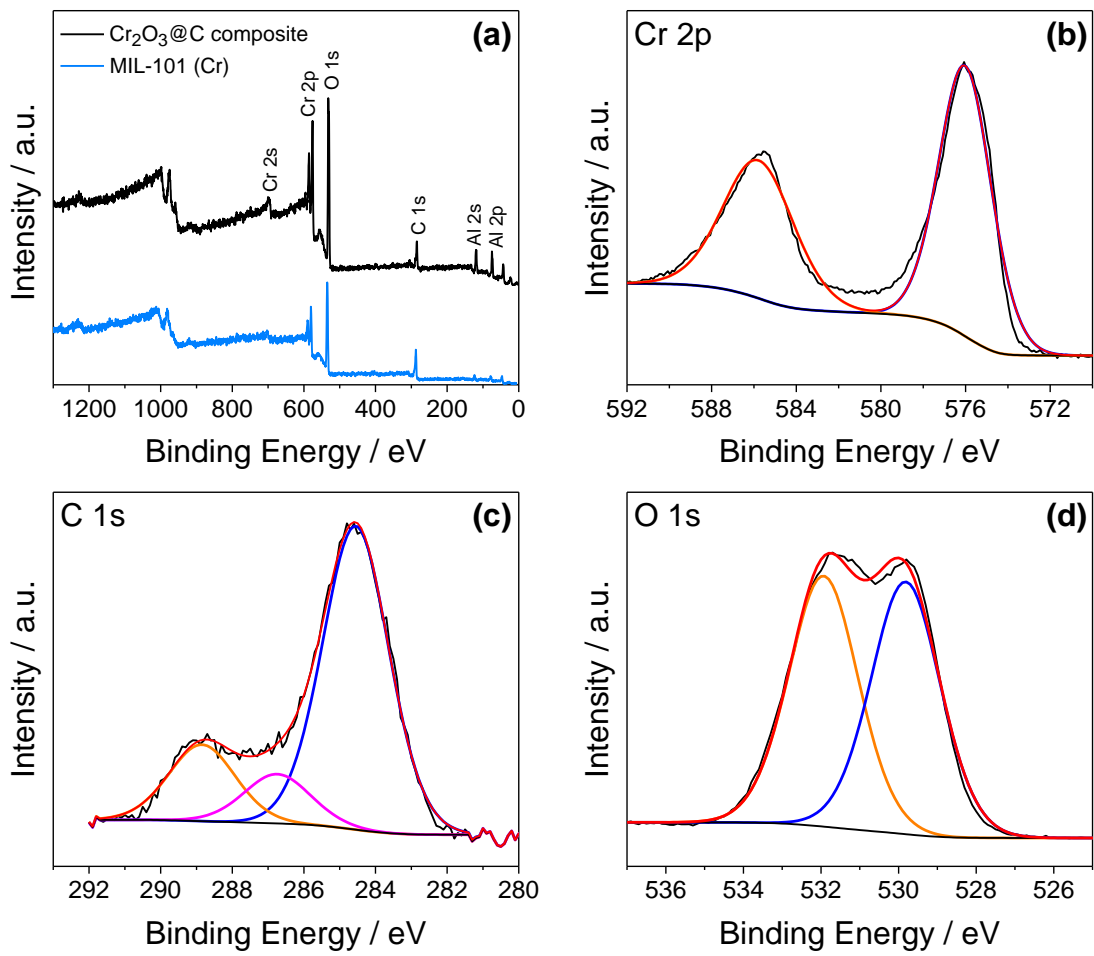


Figure 2

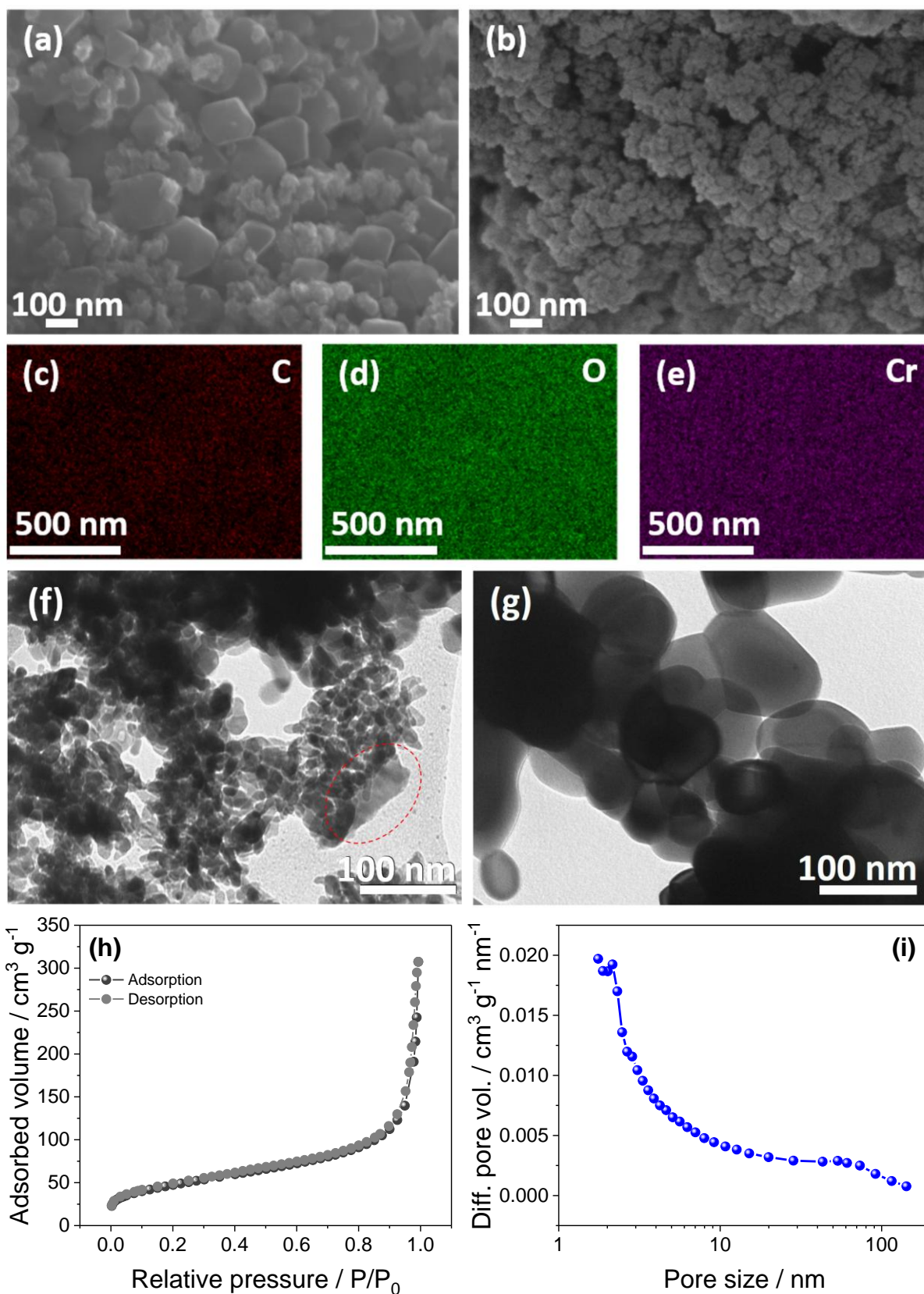


Figure 3

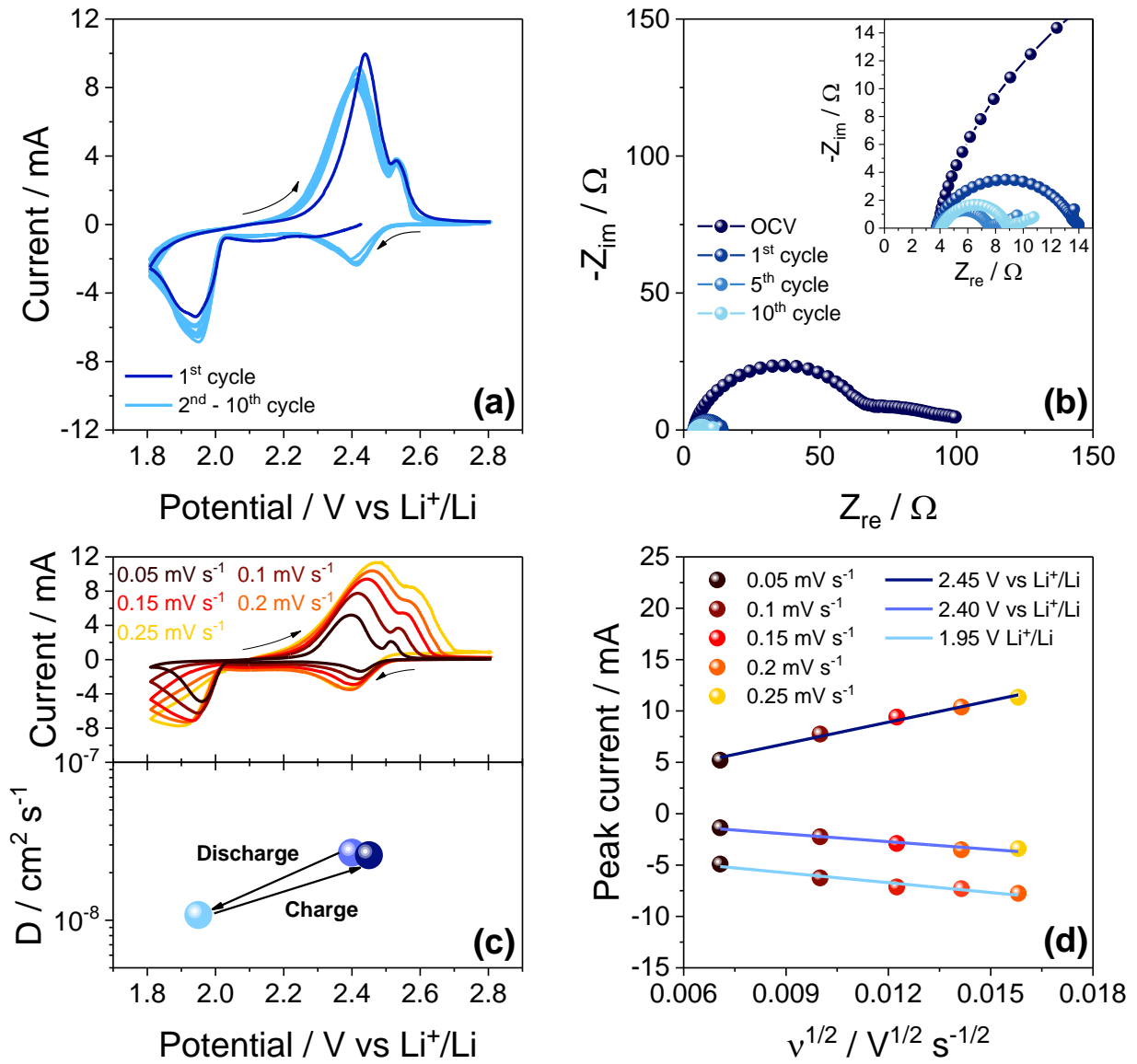


Figure 4

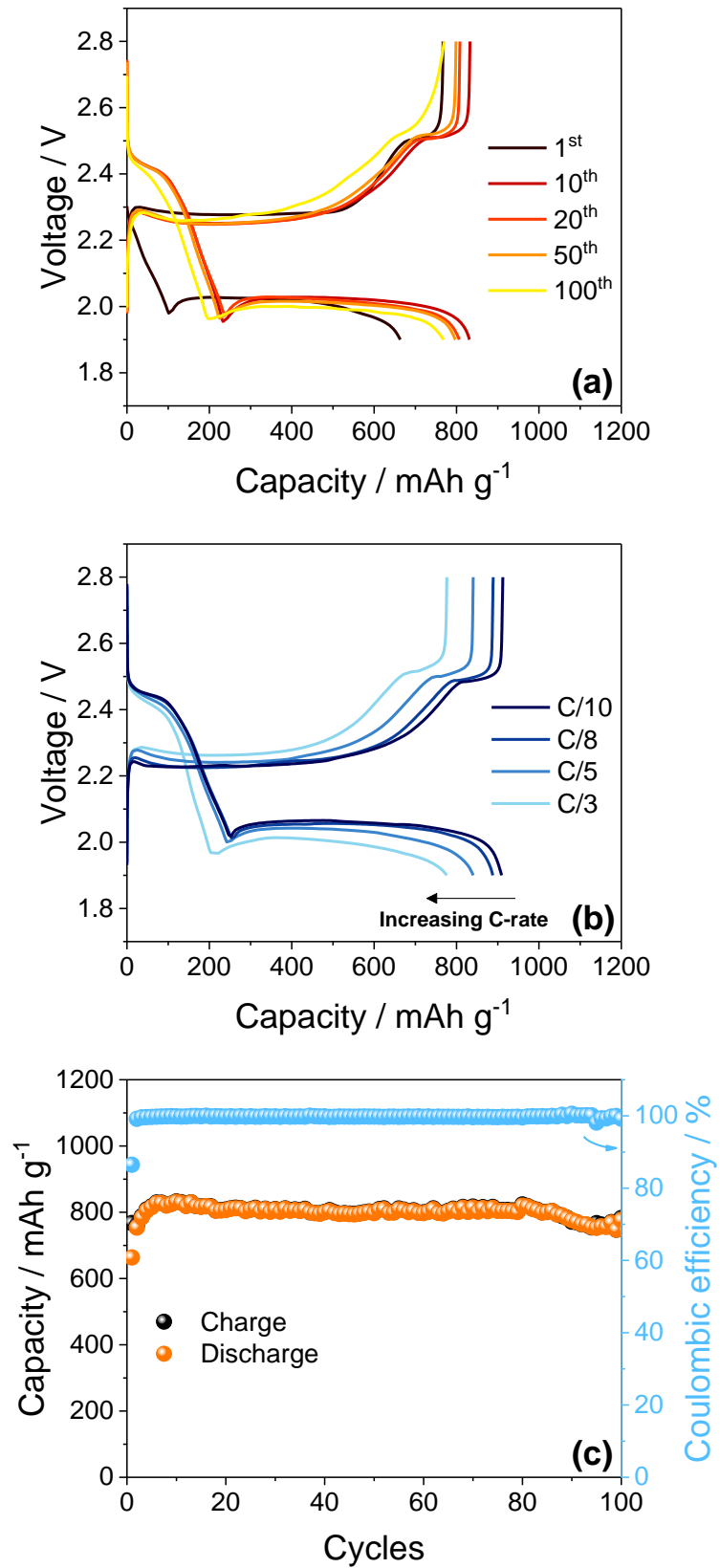


Figure 5

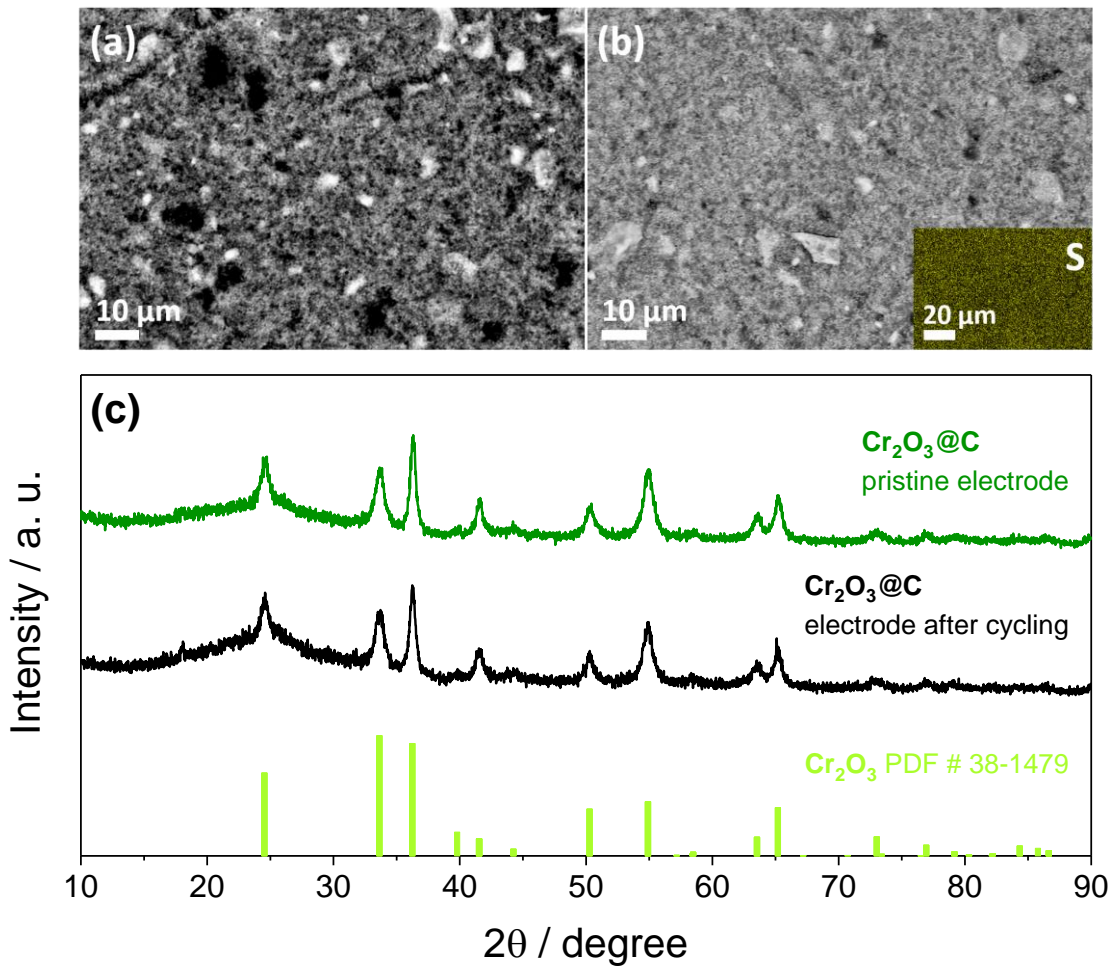


Figure 6